RAMAN SPECTROSCOPY FOR THE DETECTION OF CANCERS AND PRECANCERS

Anita Mahadevan-Jansen and Rebecca Richards-Kortum
University of Texas at Austin, Biomedical Engineering Program, Austin, Texas 78712

ABSTRACT

Optical spectroscopy has been extensively studied as a potential *in vivo* diagnostic tool that can provide information about both the chemical and morphologic structure of tissue in near real time. Most *in vivo* studies have concentrated on elastic scattering and fluorescence spectroscopies since these signals can be obtained with a good signal-to-noise ratio quickly. However, Raman spectroscopy, an inelastic scattering process, provides a wealth of spectrally narrow features that can be related to the specific molecular structure of the sample. Because of these advantages, Raman spectroscopy has been used to study static and dynamic properties of biologically important molecules in solution, in single living cells, in cell cultures, and more recently, in tissues. This article reviews recent developments in the attempt to develop diagnostic techniques for precancers and cancers, based on Raman spectroscopy. The article surveys important transformations that occur as tissues progress from normal to precancer and cancerous stages. We briefly review the extensive literature that summarizes the features and interpretation of Raman spectra of these molecules in solution, and in progressively more complex biological systems. Finally, spectra obtained from intact tissues are comprehensively reviewed and discussed in terms of the molecular and microscopic literature to develop a framework for analyzing Raman signals to yield information about the molecular changes that occur with neoplasia. The article concludes with our perspective on the potential role of Raman spectroscopy in diagnosing precancer and cancerous tissues.

Key Words Raman spectroscopy; cancer; precancer; neoplasia; dysplasia; tissue; diagnosis.

1 INTRODUCTION

Raman spectroscopy is an inelastic scattering technique that can be used to probe the vibrational energy levels of molecules within a sample. A Raman spectrum is a plot of scattered intensity as a function of energy difference between the incident and scattered photons. The loss (or gain) in photon energies corresponds to the difference in the final and initial vibrational energy levels of molecules participating in the interaction. Typically, Raman peaks are spectrally narrow (a few wavenumbers) and in many cases can be associated with the vibration of a particular chemical bond (or normal mode dominated by the vibration of a single functional group) in a molecule.

Raman spectroscopy has been used extensively in biology and biochemistry to study the structure and dynamic function of important molecules (see, for example Refs. 1 through 3). The positions and relative intensities of various spectral bands can be used to probe primary, secondary, tertiary, and quaternary structures of large biological molecules. The fingerprint spectral region, from approximately 700 to 1900 cm^{-1}, contains a series of sharp bands that can be used to characterize a particular molecule, and in some cases to identify the composition of complex, multicomponent samples.

Based on the success of Raman spectroscopy in biology, many groups have recognized its potential in the study and diagnosis of disease. However, early attempts to measure Raman spectra of cells and tissues were hindered by two factors: (1) the highly fluorescent nature of these samples and (2) instrument limitations, which necessitated long integrated times and high power densities to achieve spectra with good signal-to-noise (S/N) ratios. Improvements in instrumentation in the past decade, particularly in the near-infrared region (NIR) of the spectrum, where fluorescence is reduced, have engendered a dramatic increase in biomedical applications of Raman spectroscopy. Several articles have recently reviewed this field,[4–6] and illustrated the diversity of potential applications, which range from monitoring cataract formation *in vivo*[4] to the precise molecular diagnosis of artherosclerotic lesions in coronary arteries.[7] Most recently, reports have begun to appear suggesting that Raman spectroscopy has the potential for being used to diagnose and study the evolution of precancerous and cancerous lesions in human tissues *in vivo*.[8–11]

In 1994, cancer was responsible for 538,000 deaths in the United States, second only to cardiovascular

Address all correspondence to Rebecca Richards-Kortum. E-mail: kortum@mail.utexas.edu

disease.[12] A reduction in the mortality of this disease has been achieved primarily through early detection and treatment. Currently, histopathologic evaluation of a directed biopsy is used to definitively diagnose and determine appropriate treatment for most precancers and superficial cancers; this requires tissue removal, which may itself alter progression of the disease.[13] Improved methods of noninvasive diagnosis that can better target tissue requiring biopsy or can accurately identify and monitor disease progression *in vivo* could dramatically improve detection and aid therapy.[14]

Unlike conventional diagnostic techniques, spectroscopic measurements of human tissue can be made without removing tissue in near real time and tissue diagnosis can be easily automated. There is much evidence to indicate that fluorescence spectroscopy of both exogenous (see, for example, Ref. 15) and endogenous chromophores can be used to identify neoplastic transformations in cells, and precancers and cancers in the breast,[16] lung,[17] bronchus,[18] oral cavity,[19] cervix,[20] and gastrointestinal tract.[21,22] Several clinical systems, based on fluorescence spectroscopy, have been successfully used *in vivo*.[21,23] However, fluorescence spectra of precancerous tissues of the cervix and colon, and benign abnormalities such as inflammation and metaplasia, are similar in some patients.[22,24] This suggests that the use of fluorescence diagnosis in a screening setting, where the incidence of precancer is expected to be low, may result in an unacceptably high flash positive rate. Only a limited number of biological molecules such as flavins, porphyrins, and structural proteins (collagen and elastin) contribute to tissue fluorescence, most with overlapping, broadband emission. In contrast, most biological molecules are Raman active, with distinctive spectra in the fingerprint region; hence, it has been suggested that vibrational spectroscopy may overcome some of the potential limitations of fluorescence diagnosis of precancers and cancers. This is supported by direct comparisons of fluorescence and Raman spectra of normal cervix, cervical precancer, and cervical tissues with inflammation, which indicate that Raman spectroscopy may provide more specific diagnosis of cervical precancers.[25]

This paper reviews the literature relevant to the development and use of Raman spectroscopy to diagnose and follow the progression of precancerous and cancerous lesions. The application of visible, Fourier transform infrared (FT-IR) and near-infrared Raman techniques is included. Although ultraviolet resonance Raman (UVRR) spectroscopy has been used extensively to study biological molecules (see, for example, Ref. 26), UV radiation may be mutagenic, potentially, precluding its use *in vivo*.[27] Therefore, UVRR studies are excluded from this review. We begin by briefly summarizing some relevant molecular and structural changes that accompany neoplastic transformation in tissues. This is followed by an overview of the extensive literature describing Raman spectra of single molecules that participate in the neoplastic process. We briefly summarize Raman spectra reported from normal and neoplastic single cells and cellular constituents; this work is discussed in the context of results from single molecules in solution. Finally, we comprehensively review Raman spectra of normal and neoplastic intact tissues, with reference to work at the molecular and microscopic levels. It is our hope that this review article will provide a framework to aid interpretation of Raman signals from neoplastic tissues and will help guide rational development of clinically useful diagnostic techniques.

2 Review of Cancer Biology

The term *neoplasia,* which literally means "new growth," is used clinically to describe pathologic tissue masses which grow independent of and faster than normal tissues.[13] A neoplasm (tumor) may be classified as benign or malignant, based on its potential to harm the host body. These designations are not rigid, in that over a period of years a benign tumor may become malignant and vice versa. Malignant tumors are also called *cancers.* The nomenclature of a neoplasm reflects its microscopic origin as well as the potential to harm the host. For example, cancers arising from glandular epithelial tissue are called *adenocarcinomas,* where the suffix carcinoma indicates epithelial origin and the prefix adeno reflects glandular origin. On the other hand, cancers arising from mesenchymal tissue are called *sarcomas.*

It is generally believed that most cancers have a monoclonal (single cell) origin.[13] This single cell can give rise to a focus of neoplastic cells; in the case of epithelial tissues, if the neoplastic cells are confined to the epithelium, the lesion is regarded as a precancer. These precursor lesions can progress by invading the basement membrane to become full cancers; however, because the incidence of precancers is so much higher than that of cancers, it is widely believed that many precursor lesions naturally regress. Neoplastic cells are characterized by increased nuclear material, an increased nuclear-to-cytoplasmic ratio, increased mitotic activity, abnormal chromatin distribution, and decreased differentiation. There is a progressive loss of cell maturation, and proliferation of these undifferentiated cells results in increased metabolic activity. Histologically, neoplasms are characterized by cellular crowding and disorganization. The increased metabolic activity induces rapid angiogenesis and results in the formation of leaky vessels.

These general features of neoplastic cells result in specific changes in nucleic acid, protein, lipid, and carbohydrate quantities and/or conformations.[13] For example, neoplastic cells are known to produce more lactate than normal cells. Several oncoproteins

that mimic the functions of normal cytoplasmic proteins have been found to be present with cancers. The DNA–protein interaction is also disturbed in malignant transformations, and nuclear proteins that normally regulate cell division and DNA replication are altered, resulting in cell proliferation. The activation of regulatory oncoproteins/oncogenes results in repeated duplication and amplification of DNA sequences. Tumor cells secrete or induce host cells to secrete proteolytic enzymes such as serine, cysteine, and metalloproteinases. Invasive carcinomas, melanomas, and sarcomas contain high levels of type IV collagenase, a metalloproteinase. Other proteins present in elevated levels in tumors include fibronectin, laminin, and protein cores of proteoglycans, which are activated by cathepsin D, a cysteine proteinase.

The morphologic and biochemical changes that occur with neoplasia are numerous and in many cases depend on the specific type and location of the cancer. Biochemical tumor markers include cell surface antigens, cytoplasmic proteins, enzymes, and hormones (Table 1).[13] For example, alpha fetoprotein (AFP) is a glycoprotein normally synthesized early in fetal life. Elevated levels of AFP are observed in patients with cancers arising in the liver and germ cells of the testis. It is less commonly present in carcinomas of the colon, lung, and pancreas. As another example, in cervical epithelium, high molecular weight keratins are unique to mature epithelium. These keratins become abnormal in mild precancers and are replaced by low molecular weight keratins in severe precancers and carcinomas. Most lung cancer patients with Cushing syndrome have elevated levels of adrenocorticotropic hormone (ACTH) and its precursor molecule, propiomelanocortin (POMC). Another paraneoplastic syndrome that accompanies cancer is hypercalcemia. This is accompanied by a parathyroid hormone-related protein that is present only in small amounts in normal cells, but is elevated with certain cancers. It should be noted that some of these markers may also be present in certain benign abnormalities such as cirrhosis or hepatitis.

In summary, there are multiple molecular markers, located in the membrane, the cytoplasm, the nucleus, and the extracellular space that may be indicative of neoplasia. Marker molecules include proteins, lipids, and nucleic acids; changes in either the marker or its interaction with another molecule may be expected.

3 RAMAN SPECTRA OF MOLECULES PARTICIPATING IN NEOPLASIA

Raman spectra have been measured and used to analyze changes in the structure and environment of many of the molecules that participate in neoplastic transformation. This section provides an overview of the structure of these molecules and

Table 1 Potential biological markers and the associated type of cancers. (Modified from Ref. 13.)

Markers	Associated Cancers
Hormones	
human chorionic gonadotropin	trophoblastic tumors, nonseminomatous testicular tumors
calcitonin	medullary carcinoma of thyroid
catecholamine and metabolites	pheochromocytoma and related tumors
Oncofetal Antigens	
alpha-fetoprotein	liver cell cancers, nonseminomatous germ cell tumors of testis,
carcinoembryonic antigen	carcinomas of colon, pancreas, lung, stomach and breast
Isoenzymes	
prostatic acid phosphatase	prostate cancer
neuron-specific enolase	small cell cancer of lung, neuroblastoma
Specific Proteins	
immunoglobulins	multiple myeloma and other gammaopathies
prostate-specific antigen	prostate cancer
high/low molecular weight keratins	cervical cancer
Mucins and other Glycoproteins	
CA-125	ovarian cancer
CA-19-9	colon and pancreatic cancer
CA-15-3	breast cancer

reviews features and interpretation of Raman spectra from individual molecules in solution.

3.1 PROTEINS

The structural integrity of most epithelial tissues is provided by fibrous proteins within the stroma. Collagen and elastin fibers form a network that supports the basement membrane and epithelial cells. In addition, globular proteins play important roles within the epithelial cells; for example, DNA is bound to small proteins known as histones to form chromatin within the nucleus.[28]

Raman spectroscopy can be used to probe protein structure at several different levels (see, for example, Refs. 1 through 3 and 29). Proteins are made up of amino acids linked together by amide (pep-
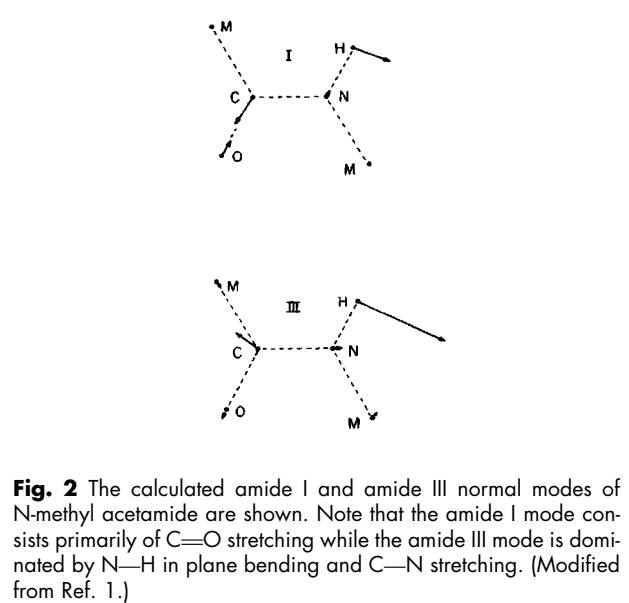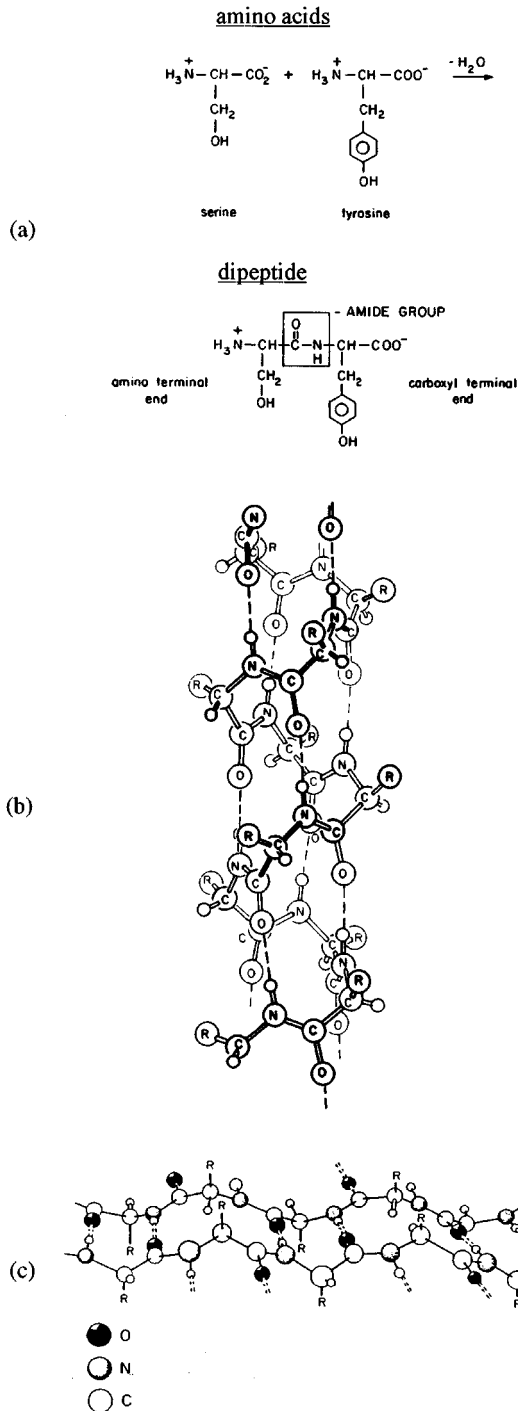
amino acids

(a)

dipeptide

(b)

(c)

Fig. 1 (a) Two amino acids (serine and tyrosine in this example) are joined via an amide group to form a dipeptide. (b) Proteins can exist in the α-helix conformation, where the amino acids are arranged in a helix about the long axis of the protein. (c) Polypeptide chains can interact to form parallel or anti-parallel β-pleated sheets. (Modified from Ref. 1.)

Fig. 2 The calculated amide I and amide III normal modes of N-methyl acetamide are shown. Note that the amide I mode consists primarily of C=O stretching while the amide III mode is dominated by N—H in plane bending and C—N stretching. (Modified from Ref. 1.)

chain along the long axis of the protein. In the α-helix form, hydrogen bonds between every third amide residue hold the protein in a helix, with approximately 3.6 amino acids per turn of the helix [Fig. 1(b)]. Alternatively, individual polypeptide chains can form hydrogen bonds with a second chain, either in a parallel or antiparallel fashion, to form β-pleated sheets [Fig. 1(c)]. Tertiary structure describes the tightly folded three-dimensional structure of globular proteins. These proteins have domains characterized by predominantly α-helical or β-pleated structure, but can also contain large regions that appear to have a random structure. This three-dimensional structure is stabilized by covalent interactions between individual polypeptide chains. For example, —S—S— crosslinks may form from two cysteine residues, or individual proteins may be bound to a prosthetic group such as the prophyrin moiety in heme proteins. Finally, quaternary structure describes the integration of protein monomers and/or prosthetic groups to form functional biological units such as complex enzymes, hemoglobin, and collagen fibers.

Raman spectra of proteins in the fingerprint region contain information about the primary, secondary, tertiary, and quaternary structure of proteins (see, for example, Refs. 1 and 3). Various amino acids, which are important in primary structure, can be characterized by their vibrational spectra, including tyrosine with peaks at 830 and 850 cm^{-1}, tryptophan with peaks at 1014, 1338, 1361, and 1553 cm^{-1}, and phenylalanine with a peak at 1006 cm^{-1}. Secondary protein structure significantly influences the Raman spectrum of the peptide backbone. The amide linkage between amino acid residues has four normal modes, two of which are Raman active (Fig. 2): the amide I mode, which is largely due to C=O stretching, and the amide III mode, which is due to C—N stretching and N—H

tide) bonds [Fig. 1(a)].[28] The primary structure of the protein is determined by the sequence of amino acids. The arrangement of proteins in three dimensions is termed secondary structure, which essentially describes the arrangement of the polypeptide

Table 2 Locations of amide I, amide III, and skeletal C—C peaks in Raman spectra of proteins with various secondary structures.

Proteins	Amide I (C=O)	Amide III (C-N, N-H)	Skeletal (C-C)
α-helix	1654-1662	1258-1304 (weak)	935-945
β-sheet	1665-1680	1227-1247	1002
Unordered	1654-1685	1235-1270	1100-1110

in plane bending. The position of the amide I and amide III peaks as well as the skeletal C—C vibrations near 900 to 980 cm^{-1} can be used to characterize the secondary structure of protein.

Table 2 and Figure 3 characterize the positions of vibrations for protein conformations with various secondary structures, and indicate characteristic vibrational spectra of the α-helix, β-pleated sheet and random coil configurations. Figure 3 shows that the amide I and III peaks of proteins in the α-helix conformation are distinct from those of other conformations. The overlapping amide I and III bands of the β-pleated sheet and undefined forms have distinct line shapes. Various quantitative methods have been proposed to calculate the proportion of protein in the α-helix, β-pleated sheet and undefined conformations based on the intensity, positions and shape of the amide I and III bands.[30–34] The C—H deformation vibration of the methylene group at 1448 to 1459 cm^{-1} is relatively conformation insensitive and has been proposed as an intensity standard in some of these methods. Disulfide bridges, which are important in the tertiary structure of a protein, contribute to the Raman spectrum from 500 to 550 cm^{-1}. Finally, individual prosthetic groups, which are important in the quaternary structure of a protein, can contribute significantly to the Raman spectrum, although this contribution is so dependent on the nature of the prosthetic group that no general rules can be assigned.

Figure 4 shows the Raman spectra of two important structural proteins in tissue: collagen and elastin.[8] Table 3 lists the positions of vibrations for these proteins.[2,8] The spectrum of elastin shows strong amide III (1250 cm^{-1}) and amide I (1660 cm^{-1}) vibrations and weak skeletal C—C peaks, reflecting the disordered structure of this protein.[2] In contrast, the collagen spectrum shows a strong amide I peak at 1650 cm^{-1} and two amide III peaks at 1250 and 1270 cm^{-1}, which are attributed to the polar and nonpolar regions of the triple helix conformation.[2] Note that the relative intensity of the amide peak to the CH_2—CH_3 peak at 1450 cm^{-1} is less than one in elastin and greater than one in collagen.[8]

3.2 DNA

Nucleic acids, such as DNA, are built from nucleotides, which consist of a phosphorylated sugar attached to a purine or pyrimidine base (Fig. 5).[28] Purine bases are adenine and guanine, and pyrimidine bases are cytosine and thymine in DNA, and cytosine and uracil in RNA. β-D-2-Deoxyribose is the sugar found in DNA; β-D-ribose is the sugar found in RNA. Hydrogen bonds between complementary base pairs (adenine–thymine and guanine–cytosine in DNA) stabilize the double-stranded helical forms of DNA. In addition, interactions between bases, which are stacked up along the long axis of the helix, stabilize the conformation. DNA can exist in several double helix conformations: A, B, C, and Z (Fig. 6). The B form of DNA, described by the original Watson–Crick model, is the most abundant in
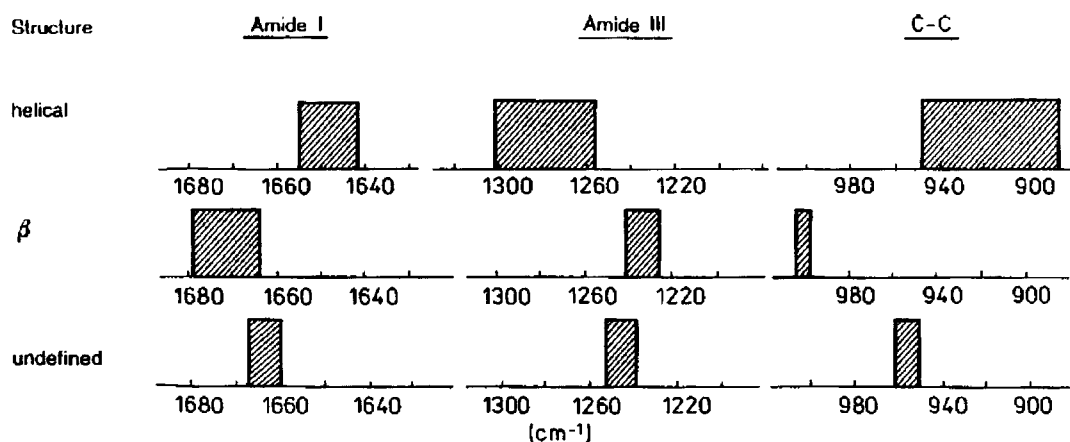
Fig. 3 Range of positions of amide I, amide III, and skeletal CC vibrations for proteins with various secondary conformations. (Modified from Ref. 3.)
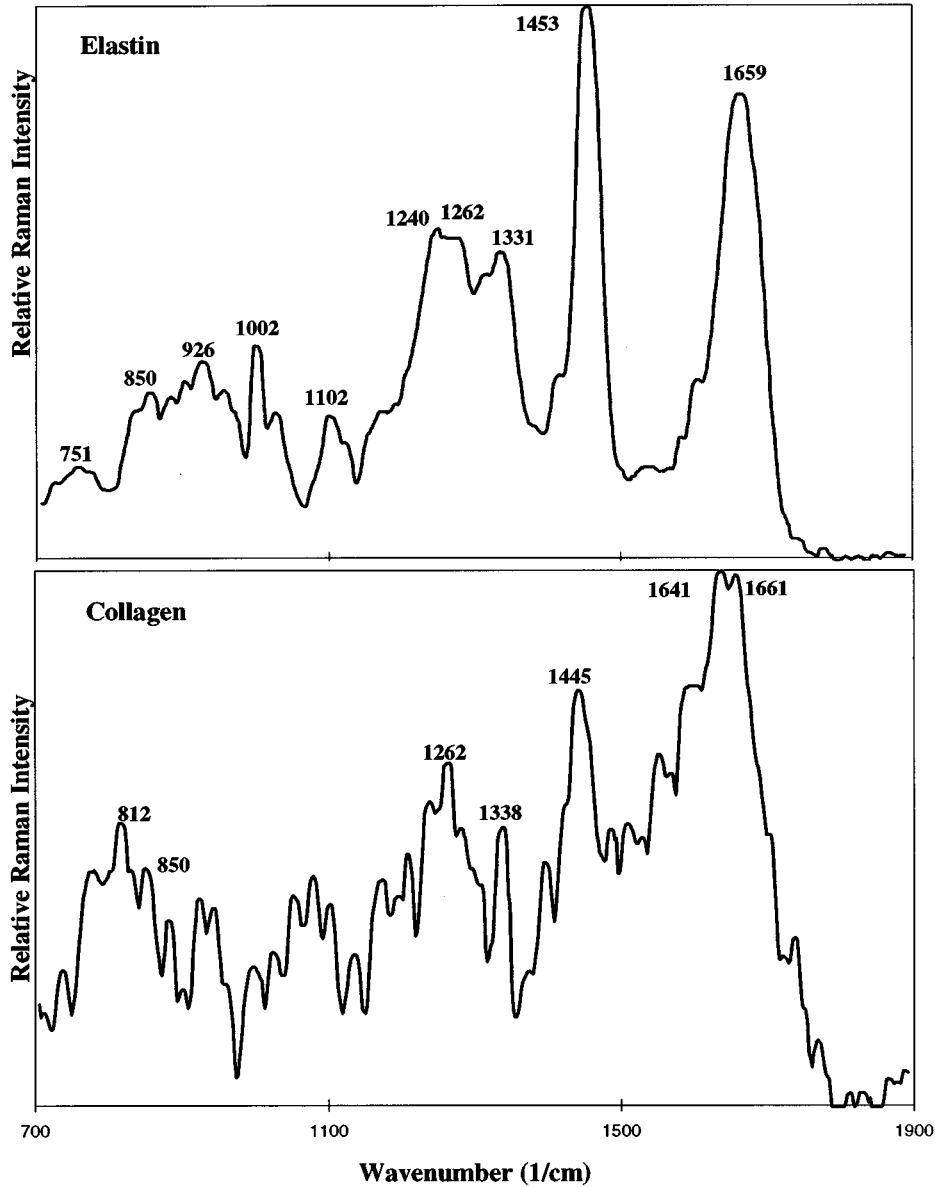
Fig. 4 FT-IR Raman spectra of (a) collagen and (b) elastin (1064 nm excitation, 10 W/cm², 15 min). (Modified from Ref. 8.)

aqueous solutions and is a right-handed helix.[35,36] A and C forms are also right handed; A form DNA is observed at lower relative humidities. Z form DNA is left handed and occurs when the double helix is unwound for genetic expression. DNA undergoes a transition from the B to Z form at high ionic strengths.

The use of Raman spectroscopy in analyzing DNA conformation has been reviewed recently.[37] It has been shown that Raman spectroscopy can be used to determine whether DNA is in the A, B, C, or Z conformation. Most DNA in the cell exists in the B form; however, the B form of DNA is not one structure, but rather a family of structures, which depend on the base sequence, the location and extent of bound water, the ionic environment, and the presence of interacting proteins (see, for example,

Table 3 Locations of various peaks in the Raman spectra of collagen, elastin, and histones. (Assignments from Ref. 2.)

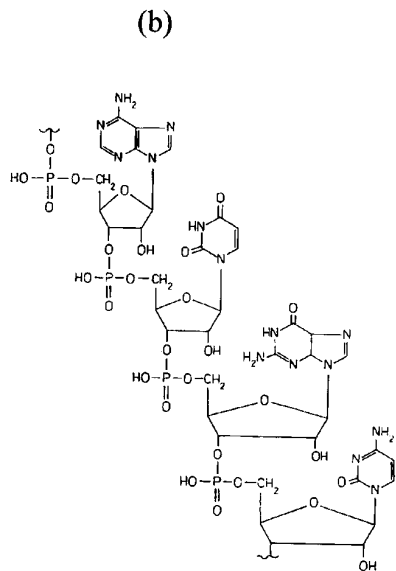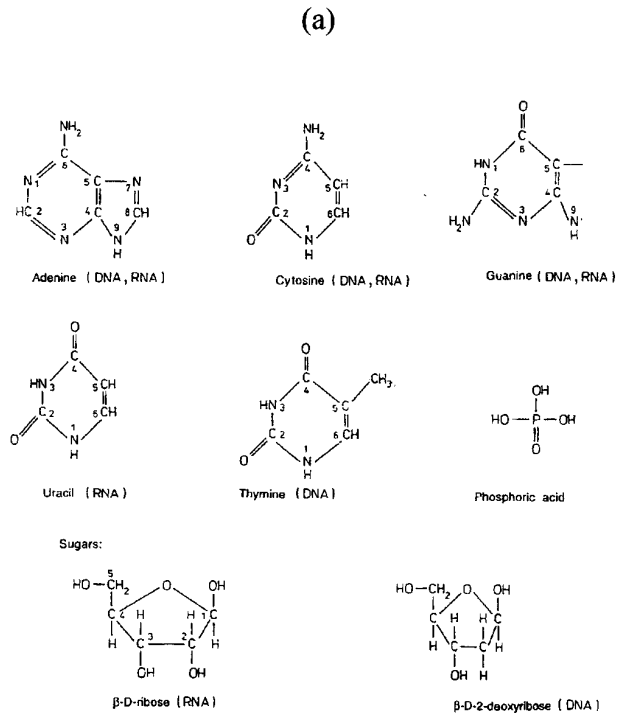| Protein	Amide I	Amide III	Other
Collagen	1670 (s)	1271 (s)	1006 (m) phenylalanine
	1642 (sh)	1248 (s)	938 (m) protein backbond
			921 (m) proline ring
Elastin	1668 (s)	1254 (s)	938 (w)
Histones	1648-1661	1245-1305	647-654
			743-752
			825-830 tyrosine
			854-856 tyrosine
			1006 phenylalanine
			1451-1454 CH₂ bend

(a)

(b)

Fig. 5 (a) The components of nucleic acids: adenine and quanine (purines); cytosine, uracil, and thymine (pyrimidines); β-D-ribose and β-D-2 deoxyribose (sugars); and phosphoric acid. (b) A fragment of an RNA chain; nucleotides, consisting of a base and a phophorylated sugar, are linked via the phosphoric acid moiety. (Modified from Ref. 3.)

Fig. 6 Schematic diagram illustrating the four conformation of DNA and expected Raman spectra from 600 to 900 cm^{-1} for each. The O-P-O band is present at ~830 cm^{-1} in B DNA, at ~805 cm^{-1} in A DNA, at ~785 cm^{-1} in C DNA, and at ~748 cm^{-1} in Z DNA. (Modified from Ref. 3.)

Refs. 35 and 36). Raman spectroscopy can be used to probe subtle changes in B form DNA.

In general, bands in the Raman spectrum of DNA can be assigned to vibrations predominantly of either the sugar phosphate backbone or one o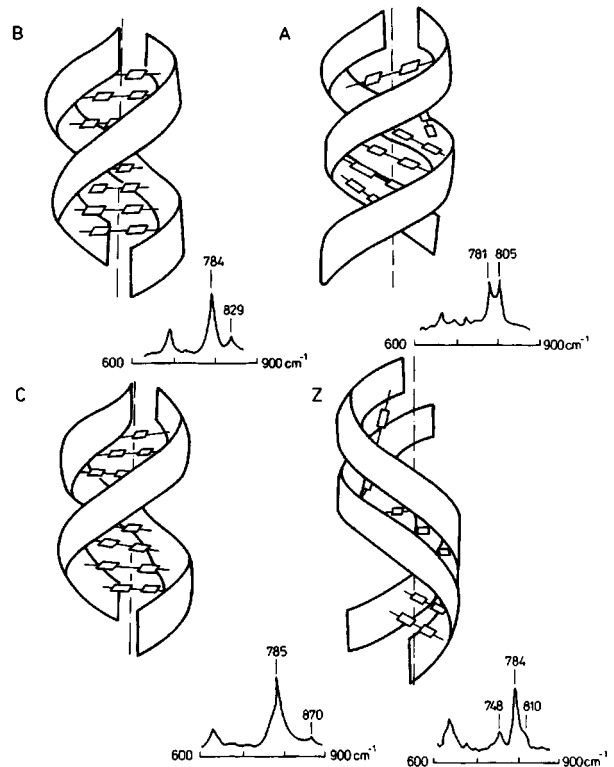f the four bases (Fig. 7).[37,38] The region from 500 to 800 cm^{-1} is full of weak lines due to the vibrations of heterocyclic rings of the bases: there is a strong line at 770 cm^{-1} due to breathing of the aromatic ring of pyrimidine bases (C,T), and a moderately strong line at 670 cm^{-1} due to purine bases (A,G). The region from 1100 to 1700 cm^{-1} is also rich in bands due to base vibrations. Pyrimidine bases (C,T) have a characteristic vibration at 1240 cm^{-1}, while both purines (A,G) have vibrations at 1480 and 1570 cm^{-1}. The O-P-O stretching vibration is located near 800 cm^{-1}, although its exact position is conformation sensitive. The sugars contribute weak bands from 800 to 1100 cm^{-1} as well as a pentose vibration at 1460 cm^{-1} due to CH$_2$ deformations.

Figure 8(a) shows Raman spectra of DNA in various conformations; the marker bands are shaded.[37] Table 4 and Fig. 8(b) summarize the positions of these bands for the various forms of RNA and DNA. The relative positions and intensities of these marker bands can be used to differentiate among the various forms of DNA as well as to understand the origin of spectral differences among various B conformations. There are three main backbone vibrations which are conformationally sensitive: (1) The symmetric stretching of the two ionized phosphate oxygens in the diphosphate ester is near 1100 cm^{-1} in the A form and at 1095 cm^{-1} in the B form.
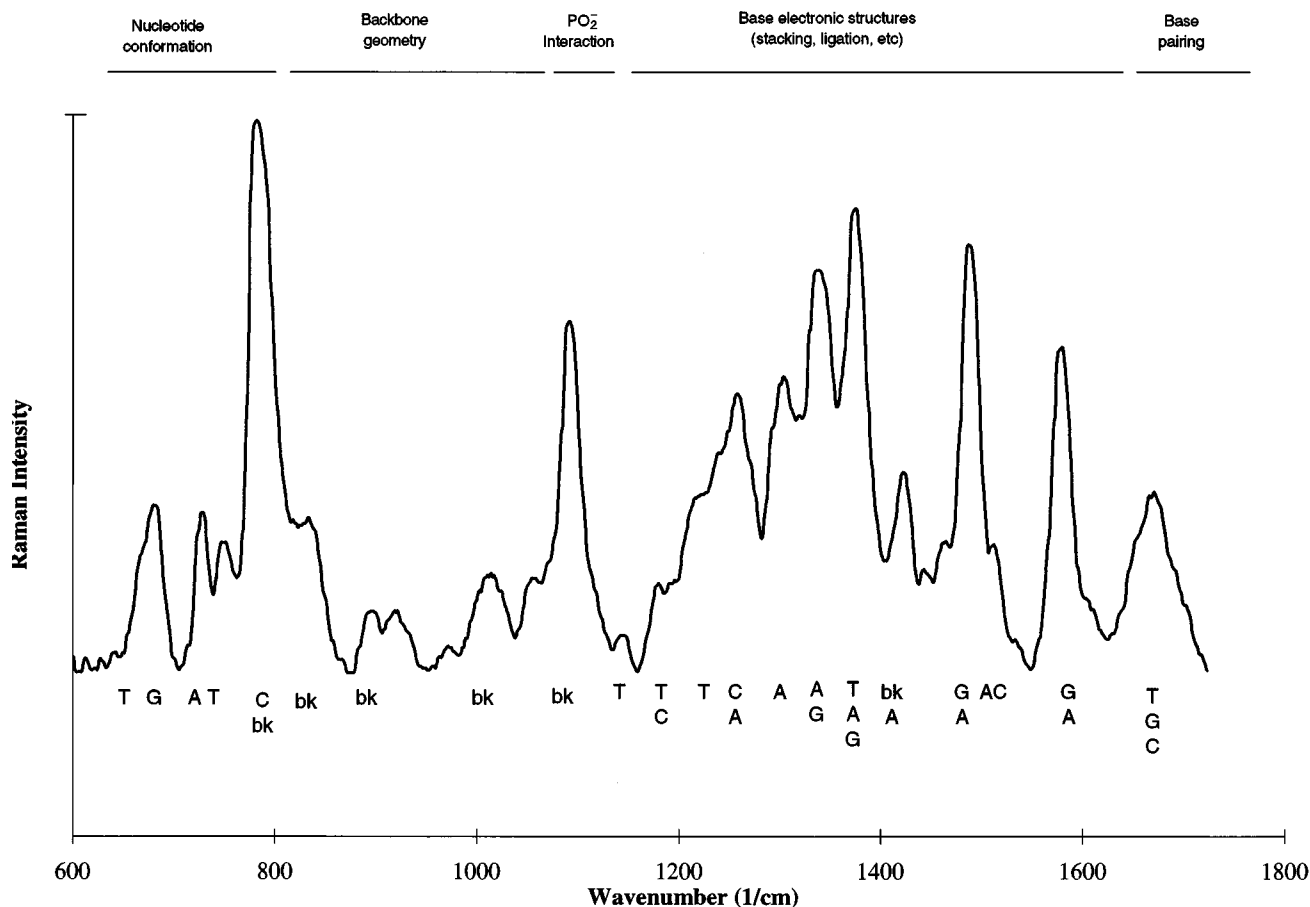
Fig. 7 Typical Raman spectrum of calf thymus B form DNA. Peaks from 600 to 800 cm^{-1} are due to the bases and are sensitive to DNA conformation. Peaks from 800 to 1100 cm^{-1} are sensitive to backbone geometry. The PO$_2^-$ group contributes from 1100 to 1150 cm^{-1}. Peaks from 1150 to 1600 cm^{-1} are due to bases that are sensitive to base electronic structures and are influenced by base stacking. The carbonyl region from 1650 to 1750 cm^{-1} is sensitive to base pairing interactions. (Modified from Ref. 38.)

The intensity of this vibration is independent of conformation, and thus has been suggested as an intensity standard. (2) The O-P-O symmetric stretching between the C3′ terminal of one nucleotide and the C5′ terminal of a second nucleotide is loosely referred to as the A marker band. It is found at 814 cm^{-1} in RNA (which exists in the A conformation) and at 809 cm^{-1} in A form DNA. The intensity of this band is weak in B DNA. (3) Finally, the asymmetric stretching vibration of O-P-O is located at 835 cm^{-1} in B DNA.

Because the vibrations of some of the bases are tightly coupled to the backbone, the vibrational frequencies of these bases are also sensitive to changes in the DNA conformation.[3,37] The intensity of the ring breathing mode of guanine bases is tightly coupled to backbone vibrations. The position of this peak is sensitive to the angle about the glycosidic bond [characterized as anti or syn; Fig. 9(a)] and the conformation of the sugar (characterized as C3′ endo or C2′ endo [Fig. 9(b)]) to which it is attached. In the C3′ endo/anti form, the guanine peak is at 668 cm^{-1}; in the C3′ endo/syn form it is at 625 cm^{-1}, and in the C2′ endo/anti form it is at 682 cm^{-1}. Base

pairing, which involves the formation of hydrogen bonds between keto groups of bases, can change the carbonyl portion of the vibrational spectrum (which occurs approximately at 1668 cm^{-1}). Base stacking can also both increase and decrease the intensity of vibrational lines due to the bases; for example, the guanine peak at 670 cm^{-1} increases and the adenine peak at 724 cm^{-1} decreases with increased base stacking. The extent of ordering in the DNA molecule can be monitored by the ratio of these peaks.

3.3 NUCLEAR PROTEIN INTERACTIONS

The winding of DNA about nucleosomes, which are made up of histone monomers, is the first stage in packing DNA in the nucleus.[28] Other nonhistone proteins stabilize helical arrays of nucleosomes. During cell division, or under low salt or acidic conditions, the protein–DNA interaction is altered and the packing density of DNA decreases.[28]
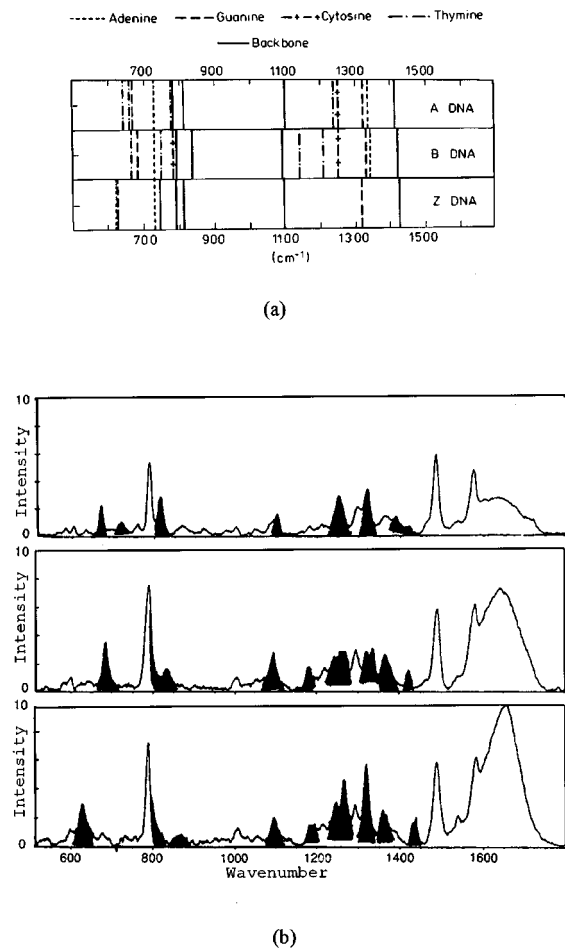
(a)

(b)

Fig. 8 (a) Positions of structurally sensitive Raman bands of A, B, and Z form DNA. (Modified from Ref. 3). (b) Raman spectra of poly GC nucleotides in the A, B, and Z forms. The marker bands are shaded. (Modified from Ref. 37.)

Table 4 Locations of various peaks in the Raman spectra of nucleic acids.

Nucleic Acid (Form)	A	C	G	T	OPO	PO$_2^-$	Deoxy-ribose
DNA (A)	727	780	666	642	806–813	1099	
	1335			1318	777		
					1239		
DNA (B)	727	782	682	665	825–842	1091	917
	1339	1250	1333	748			975
					1208		1448
							1462
DNA (C)			670		785	1090	
DNA (Z)	624		625		742–748	1095	
	729		1316				
RNA (A)	727	780	666	642	813	1099	
	1335			1318	777		
					1239		
RNA (Z)	624		640		742–748	1095	
	729		1316				

3.4 MEMBRANES

Membranes, which encase cells, are formed from bilayers of phospholipid molecules; embedded within these membranes are proteins that perform various receptor and transport functions.[1,3,28] Each phospholipid molecule contains a hydrophilic head and a hydrophobic tail; the membrane is made up of opposing layers of these phospholipids, with the hydrophobic portions of the molecule in the center (Fig. 10). The hydrocarbon chains can exist mainly in the *trans* form, with a high degree of chain ordering, or in the relatively disordered *gauche* conformation (Fig. 11). Membranes made up of phospholipids in the *trans* conformation are referred to as gels, while those with the *gauche* conformation, referred to as liquid crystals, have a greater membrane thickness. Membrane conformation is temperature sensitive and can be probed with Raman spectroscopy.

The Raman spectra of phospholipids contain vibrations from both parts of the molecule, although most peaks are due to the hydrophobic chains.[1,3]

The polar head of the phospholipid molecule has a 720 cm^{-1} peak due to C—N vibrations. The hydrophobic chains have C—C skeletal vibrations between 1000 and 1150 cm^{-1}. The intensities of these skeletal vibrations are sensitive to membrane conformation. These vibrational peaks can be used to
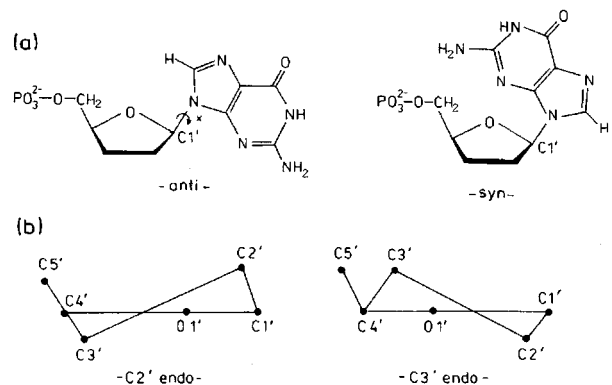

Fig. 9 The relative position of base and sugar with respect to the glycosidic bond. (a) Nucleotides can be characterized by the anti and syn configurations of the sugar and base positions with respect to the glycosidic bond. (b) Sugar ring puckering with C2' endo and C3' endo configurations exhibit distinct spectral features. (Modified from Ref. 3.)
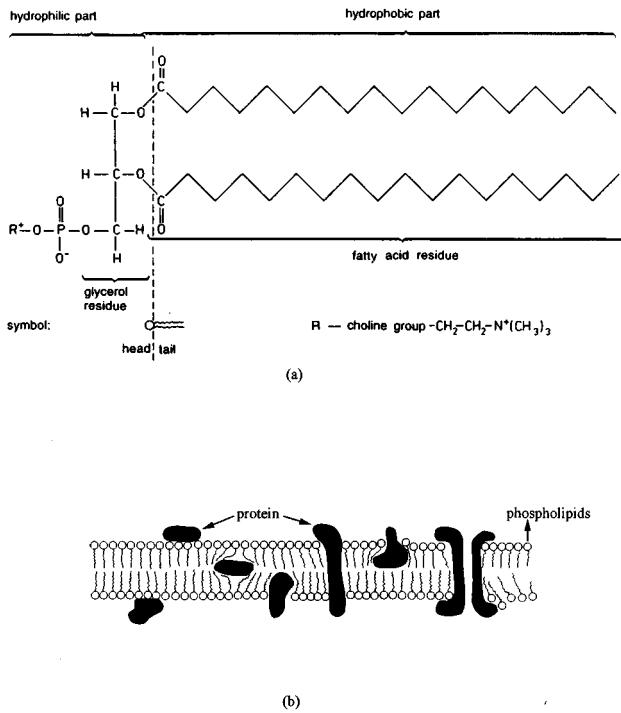
Fig. 10 (a) Lecithin, a phospholipid molecule, consists of a hydrophilic head and a hydrophobic tail. (b) biological membranes consist of opposing bilayers of phospholipid molecules. (Modified from Ref. 3.)

Fig. 12 Positions of Raman bands of membranes in the *trans* and *gauche* conformations.

quantitatively probe membrane structure; the ratios of intensities at 1064/1100 cm^{-1} and 1133/1100 cm^{-1} decrease with increasing temperature as the membrane melts (Fig. 11). C—H stretching of methylene chain groups provides two additional Raman peaks which are sensitive to both intra- and inter-chain 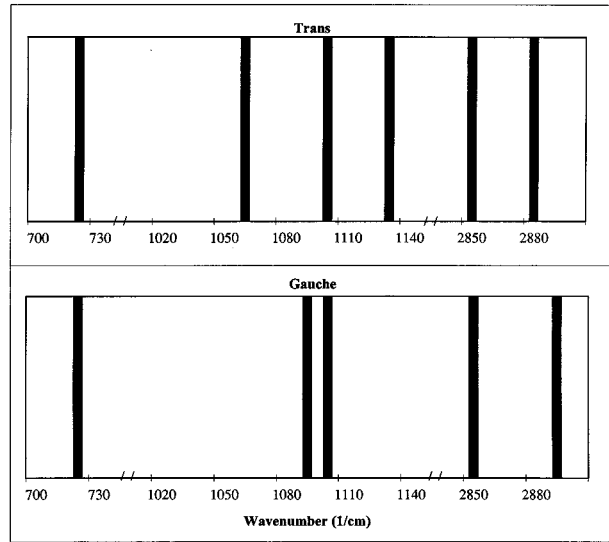interactions. The asymmetric C—H stretch occurs at 2880 cm^{-1}, while the peak due to symmetric stretching is at 2850 cm^{-1}. The ratio of intensities of these two peaks is sensitive to the density of lateral packing of hydrophobic chains and is affected by chain mobility. CH$_2$ chain deformations have a Raman peak at 1303 cm^{-1}, while =C—H deformations contribute at 1267 cm^{-1}. The ratio of intensities at these two peaks is related to the portion of unsaturated bonds in the fatty acid chains. The vibrational modes of the *cis* and *trans* isomers of C=C groups in fatty acid chains occur at 1670 to 1680 cm^{-1} and 1650 to 1666 cm^{-1}, respectively. The contributions of the various bands in membranes are summarized in Fig. 12.
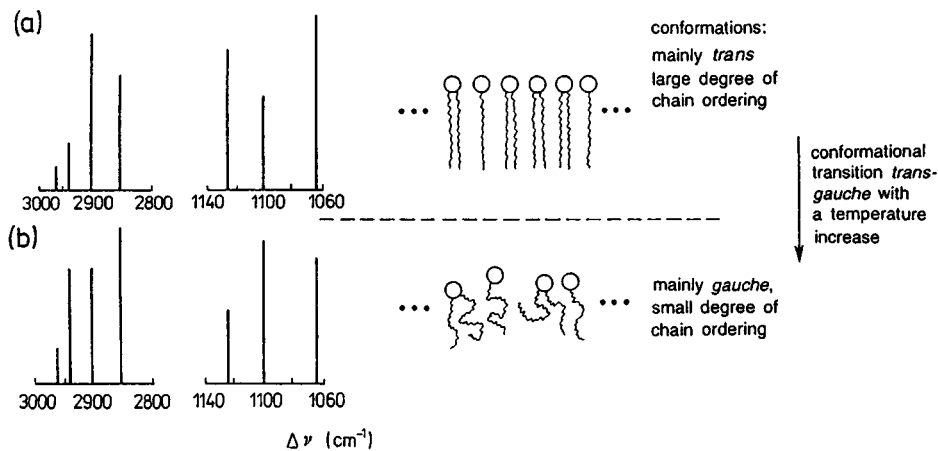

Fig. 11 Typical Raman spectra of phospholipid in the (a) *trans* and (b) *gauche* conformations. As the membrane goes from an ordered to a disordered conformation, the intensity at 1060 and 1140 cm^{-1} decreases, while that at 1100 cm^{-1} increases. The density of lateral chain packing is proportional to the ratio of the intensity at 2880 cm^{-1} to 2850 cm^{-1}. This ratio decreases as expected in the *gauche* conformation. (Modified from Ref. 3.)

4 RAMAN SPECTRA OF CELLS AND CELLULAR CONSTITUENTS IMPORTANT IN NEOPLASIA

4.1 PROTEINS

While Raman spectroscopy has been studied extensively to characterize the structure of pure proteins in solution, recently, it has also been used to study changes in protein conformation in biological systems. High levels of protein expression in many microorganisms can result in the formation of insoluble protein aggregates, or inclusion bodies. Although protein can be easily isolated from inclusion bodies, the yield of active protein can be low. Przbycien et al. examined the differences in secondary structure of β-lactamase, purified from *Escherichia coli* cytoplasm in solution and powder to that of wild-type β-lactamase, isolated from *E. coli* inclusion bodies.[39] Amide I Raman spectra were measured and analyzed using the algorithm of Williams[32] to yield the structure fractions of the α-helix content, parallel and antiparallel β-pleated sheet and random coil configuration. Figure 13(a) shows the amide I peak for each and indicates dramatic differences in the protein secondary structure. Figure 13(b) indicates that the solid pure protein has a decreased fraction of β-pleated sheet and an increased fraction of α-helix relative to the pure protein in solution. Further, the β-pleated sheet fraction of β-lactamase from inclusion bodes was increased and the α-helical content was decreased relative to pure protein, both in solution and in powder (Fig. 13). The authors conclude that these differences may reflect increased extent of protein interactions in the solid phase and in aggregates. This work shows that important structural differences may exist between pure proteins and wild-type proteins that may be sampled by Raman spectroscopy.

Zigman et al. studied UV-induced protein alterations in the lens of the gray squirrel.[40] Raman spectra were measured for a group of three controls and three UV-exposed lenses; the ratio of intensities at 2578 to 2730 cm^{-1} was used as a measure of sulfhydryl (SH) concentration, and to probe protein quaternary structure. The Raman spectra indicate that the relative contribution of sulfhydryl groups decreases with UV irradiation; this was consistent with an independent chemical analysis, which also showed an increase in protein–thiol mixed disulfides. Zigman concluded that UV irradiation makes S—H groups more reactive or oxidative.

4.2 DNA INTERACTIONS

Raman spectroscopy can be used to probe structural changes expected in the DNA of biological systems. Divalent metal cations may alter DNA structure in a number of ways and thus are potential modulators of DNA function. Raman spectroscopy has been used to study metal ion binding sites
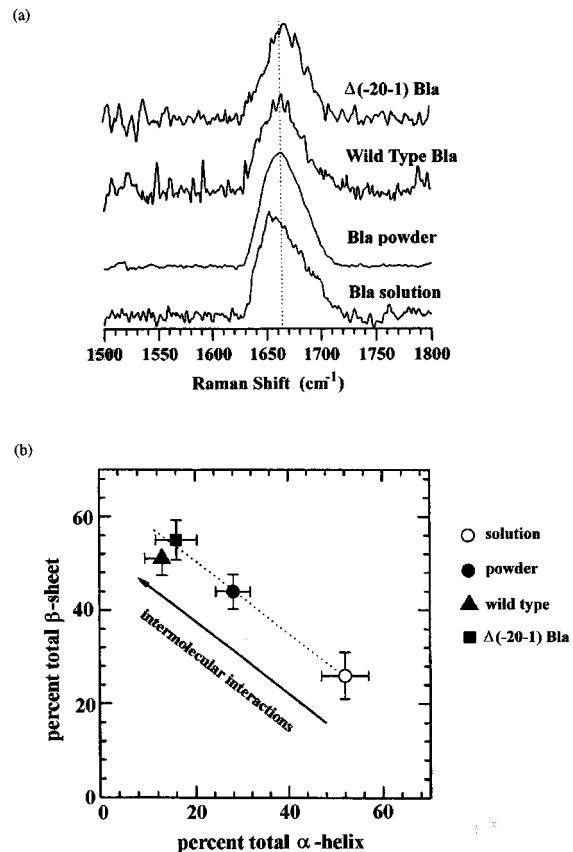

Fig. 13 (a) Fluorescence background-subtracted amide I Raman spectra of purified β-lactamase from *E. Coli* cytoplasm in solution, purified β-lactamase powder, wild-type β-lactamase powder from plasmid pKN, and purified Δ(−20−1) β-lactamase powder from cytoplasmic inclusions. Note the shift to higher wave numbers as the protein goes from solution to solid to solid from inclusions. (b) Total β-sheet content to α-helix content for samples with Raman spectra shown in (a). (○)-β la solution, ■-Δ(−20-1) β la, ●-β la powder, ▲-wild-type β la). As the protein goes from solution to solid from inclusions, the β-sheet content increases while the α-helix content decreases, reflecting increased intermolecular interactions. (Modified from Ref. 39.)

and the effect of binding on secondary and tertiary structures of DNA. Duguid and colleagues compared 514.5-nm excited Raman spectra of calf thymus DNA in the B form with that of DNA complexes with both divalent alkaline earth ions and transition metal ions.[38] From spectra of pure B form, melted DNA, and DNA–metal complexes, they calculated the percentage of nucleotide residues in B form backbone in metal–DNA complexes. Their results show that binding of alkaline earth divalent metal ions (such as Pd^{2+}) has a dramatic effect on the secondary structure of DNA measured by Raman spectroscopy, while binding transition metal ions (such as Mg^{2+}) has a much more subtle effect (Fig. 14). When calf thymus DNA was examined and analyzed, it was found to be 100% B form, with 1.5 times more guanine residues in the C2' endo/anti conformation than in the C3' endo/anti
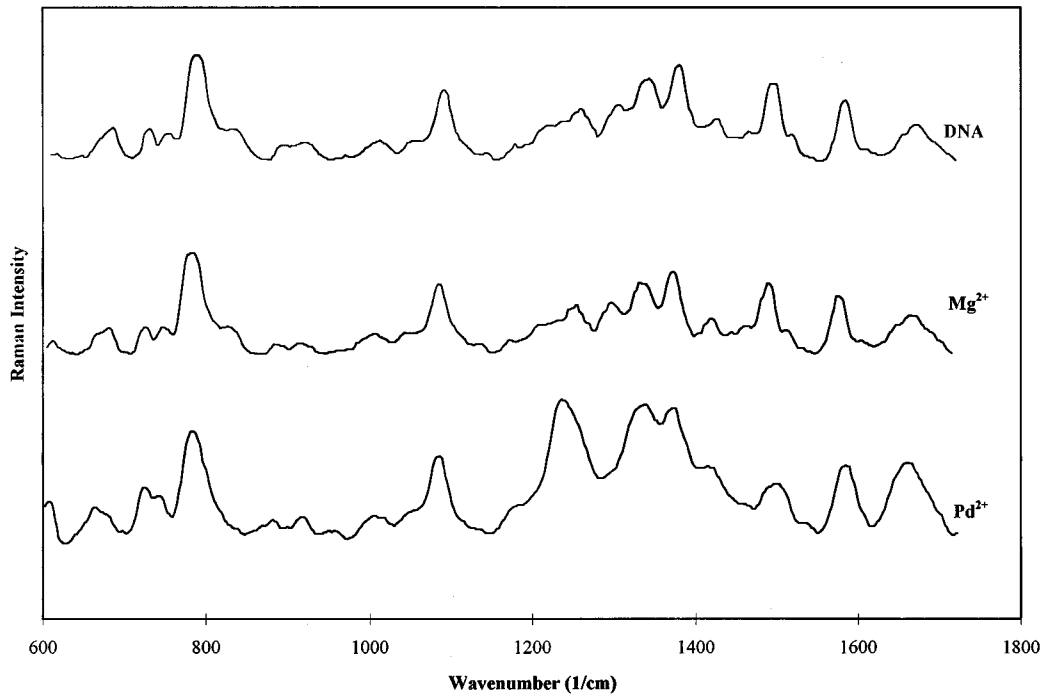
Fig. 14 Raman spectra of calf thymus DNA alone (55 mg/ml), and in the presence of Mg and Pd (100 mM). Note that the marker band at 830 cm^{-1} is conserved in the Mg spectrum but is absent in the Pd spectrum. In the Pd spectrum, the intensities at 1240 to 1260 and 1668 cm^{-1} are also markedly increased, indicating unstacking and unpairing of bases respectively. (Modified from Ref. 38.)

conformation. Mg^{2+} DNA complexes were found to have 93±9% B form, with 1.5 times more guanine residues in the C2′ endo/anti conformation than in the C3′ endo/anti conformation. However, Pd^{2+} DNA complexes had 0±17% B form structure, with only 0.7 times more guanine residues in the C2′ endo/anti conformation than in the C3′ endo/anti conformation. The authors suggest that divalent transition metals bind to purine bases and locally destabilize the helix. A number of these ions are present in biological samples and may play roles in regulating the packaging and expression of nuclear material.

Raman spectroscopy can also be used to study the interaction between proteins and DNA in biological samples. Hud and colleagues investigated the changes that occur in the secondary structure of proteins and DNA when packaged in sperm cells.[41] Sperm cells of many vertebrates use protamines, small arginine-rich proteins, to pack DNA into small volumes, protecting it from enzymatic degradation and suppression genetic activity. These workers obtained Raman spectra at 488 nm excitation for pure salmon protamine (salmine), pure B form DNA and a DNA–salmine complex (Fig. 15). They also obtained DNA spectra at a low salt concentration, which they assign a transitional B-C conformation. The Raman spectrum of the salmine–DNA complex was dominated by DNA scattering peaks [Fig. 15(a)]. The complex is less than 40% protein by weight, and DNA is a more efficient Raman

scatterer than protein at this frequency. However, the difference of the complex Raman spectrum [Fig. 15(c)] and the spectrum of pure DNA, scaled to the conformationally insensitive 1577 cm^{-1} DNA band, showed subtle differences in the secondary structure of both the protein and the DNA. The spectrum of the DNA–protamine complex shows a guanine band at 680 cm^{-1}, which is indicative of B form DNA. The phosphate backbone peak of the complex is located at 830 cm^{-1}, which is consistent with B DNA; however, this peak is weak. The difference spectrum obtained when the spectrum of pure B DNA or B-C DNA is subtracted from the spectrum of the complex indicates that the conformation of the DNA in the complex is more similar to that of pure B-C DNA. This difference spectrum [Fig. 15(e)] contains lines mainly due to the protamine, and comparing this difference spectrum with that of the pure protein [Fig. 15(f)] yields information about the changes that occur to the protein upon binding. Pure protein has an amide I peak near 1670 cm^{-1}, which indicates a β-pleated sheet conformation. However, the bound protein has an intense amide I peak at 1683 cm^{-1}. This peak is not consistent with either the α-helix or β-pleated sheet conformation, and indicates a regular secondary structure not yet characterized.

In complex biological systems containing both proteins and nucleic acids, bond assignments can be difficult due to overlapping bands. The study of bacteriophages by Raman spectroscopy provides a
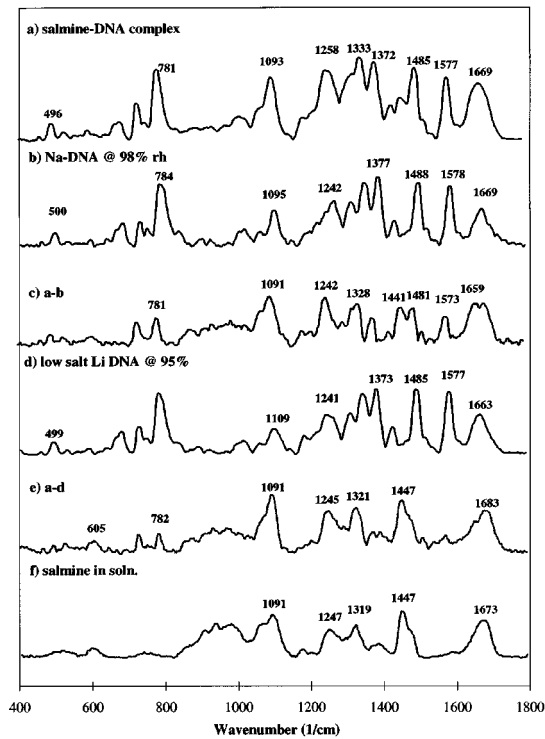
Fig. 15 Baseline-subtracted Raman spectra of (a) salmine–DNA complex at 98% relative humidity (rh); (b) Ma-DNA at 98% rh, mostly in the B form; (c) difference spectrum of (a) and (b); residual protein and nucleic acid bands are seen; (d) spectrum of low-salt LiDNA which exists in the B-C form; (e) difference spectrum of (a) and (d) which contains primarily protein bands and indicates that the DNA in the complex is similar to the B-C transitional form; and (f) spectrum of pure salmine. A comparison of (e) and (f) shows subtle changes in the protein when complexed to DNA. (Modified from Ref. 41.)
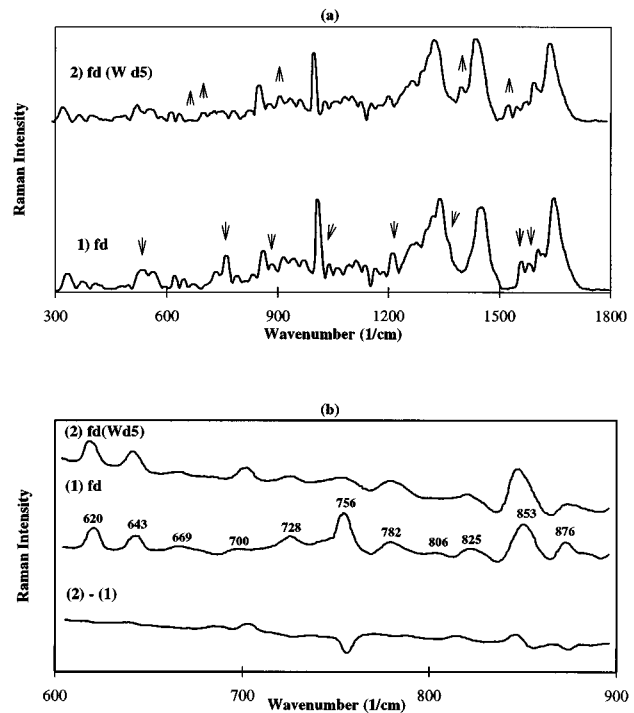

Fig. 16 (a) Solvent-corrected Raman spectra of normal filamentous bacteriophage (fd) and fd where the single tryptophan residue in the coat protein has been deuterated. The arrows in the normal fd spectrum indicate peaks assigned to tryptophan and the arrows in the deuterated fd spectrum indicate peaks assigned to deuterated tryptophan. (b) Raman spectra from 600 to 900 cm^{-1} of normal fd, fd with deuterated tryptophan, and their difference. Note that the intense tryptophan peak at 756 cm^{-1} is eliminated. The underlying band at 750 cm^{-1} is assigned to DNA. (Modified from Ref. 41.)

good illustration of this difficulty. Filamentous bacteriophages consist of a long, thin protein cylinder encapsulating a single-stranded DNA (ssDNA) loop. While the Raman spectra of ssDNA and the coat protein can be obtained individually in solution, the Raman spectra of intact bacteriophages show some important differences in DNA bands which are indicative of protein–DNA interactions.[42] The interpretation of the bacteriophage Raman spectrum (Fig. 16) is complex because there are a number of overlapping bands due to DNA and the coat protein, making unambiguous band assignment difficult. The spectral region from 600 to 900 cm^{-1} contains many conformation-sensitive bands of ssDNA. However, the intense Raman bands of the normal tryptophan residue lie in this region. Aubrey incorporated protein subunits with deuterated tryptophan to refine band assignments in this region.[42] Figure 16(a) shows the spectra of normal bacteriophage and bacteriophage with deuterated tryptophan; the difference spectrum from 600 to 900 cm^{-1} [Fig. 16(b)] clearly demonstrates the shift in vibrational frequency of tryptophan from 756 to 817 cm^{-1} with deuteration. A residual band at 750 cm^{-1} remains, following incorporation of the deuterated

tryptophan; this is assigned to DNA. Further, there is no change in intensity of the weak band at 806 cm^{-1} upon deuteration of the tryptophan, indicating that this band is also due to DNA. This work has two important implications for the use of Raman spectroscopy for diagnosis of cancer. The first is that interactions among various Raman-active constituents can affect the spectrum and this can potentially be exploited for diagnostic purposes. The second is that individual band assignments for complex biological systems can be conformed using site-directed changes that perturb the vibrational character in a predictable way without affecting conformation or assembly characteristics.

The double-stranded DNA in icosahedral viral capsids is highly condensed, and has been compared to condensed DNA in eukaryotic chromatin. Aubrey, Casjens, and Thomas used 514.5 nm excited Raman spectroscopy to contrast the secondary structure of packaged (condensed) DNA and unpackaged DNA from viral capsids.[43] Spectra were measured from an intact viral capsid, the empty protein shell, and pure, unpackaged DNA. The difference of the intact capsid and the empty shell
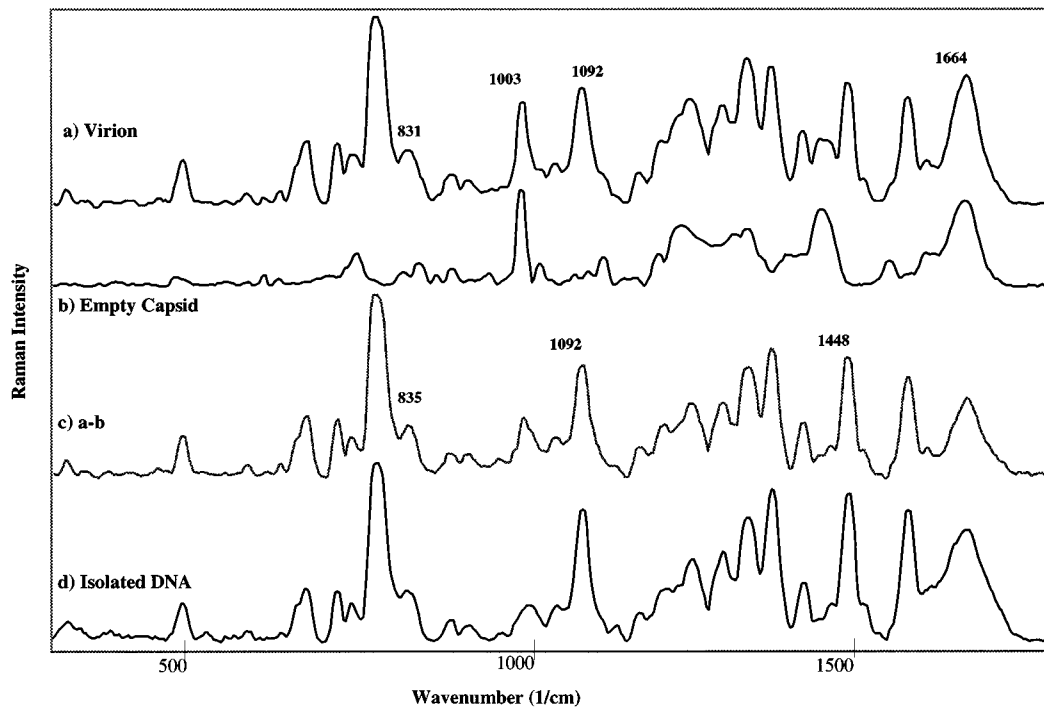
Fig. 17 Raman spectra of (a) pure virion and (b) isolated protein from virion; (c) difference spectrum of (a), (b), and (d) isolated DNA spectrum from virion. The difference spectrum shows that the spectra from packaged and isolated virion DNA are similar, indicating primarily B form DNA. (Modified from Ref. 43.)

yield the spectrum of packaged DNA, which was contrasted to that of unpackaged DNA. The Raman spectrum of an intact capsid (Fig. 17) is dominated by the peaks of DNA; although the capsid is 44% protein by weight, DNA is a more intense Raman scatterer. The spectra of packaged and unpackaged DNA are very similar (Fig. 17) but are not identical. Both exist primarily in the B form, but the difference spectrum reveals an approximately 20% decrease in the intensity of the 1092 cm^{-1} symmetric stretching mode of the PO_2^- band of B DNA when the DNA is packaged. This is interpreted to reflect an order of magnitude increase in the local Mg^{2+} concentration of packaged DNA. Mg^{2+} electrostatically shields the negatively charged phosphoxy group, reducing the molecular polarizability and thus the intensity of Raman scattering.

Puppels and colleagues recorded Raman spectra of polytene chromosomes at neutral and a series of increasingly acidic pHs.[44] They used features of the Raman spectrum to monitor DNA protein association in the chromosome, and to follow base unstacking and base protonation as the DNA takes on non-B forms. Non-B forms of DNA may play an important role in the regulation of the cell *in vivo*. Fluorescent-labeled monoclonal antibodies for Z form DNA are available, and have been used to study chromosomes under physiologic conditions. Antibody staining increases with acid fixation, indicating either that acidic conditions are favorable for the formation of Z DNA or that chromatin proteins, which dissociate at low pH, block antibody binding. Puppels showed that using confocal microspectroscopy, Raman spectra can be used to monitor the protein/DNA ratio, and the unstacking and protonation of each base type to yield information about the form of DNA as a function of pH.

Figure 18 shows Raman spectra of polytene chromosomes at neutral pH and pH 1.8 as well as the difference spectrum. Lines from 600 to 1100 cm^{-1} are primarily sensitive to base unstacking, with a decrease at 681 cm^{-1} representing guanine unstacking, and increases at 729, 749, and 784 cm^{-1} representing base unstacking of adenine, thymine, and cytosine, respectively. The decrease in protein associated with the chromosomal DNA is reflected by the decrease in the intensity of the CH_2—CH_3 protein contribution at 1449 cm^{-1}. Table 5 shows the ratio of protein to DNA content. The base vibrations from 1200 to 1700 cm^{-1} are sensitive to both protonation and unstacking. The peak at 1004 cm^{-1} is due to phenylalanine, and the change in intensity of this band reflects a change in its chemical microenvironment, possibly due to ring unstacking. The peak at 830 cm^{-1} is consistent with the phosphate backbone of the B form; the drop in intensity of this peak reflects the loss of B form structure. Table 6 summarizes the spectral changes observed at acidic conditions.

Most experiments with DNA in solution have been conducted with argon ion laser excitation.
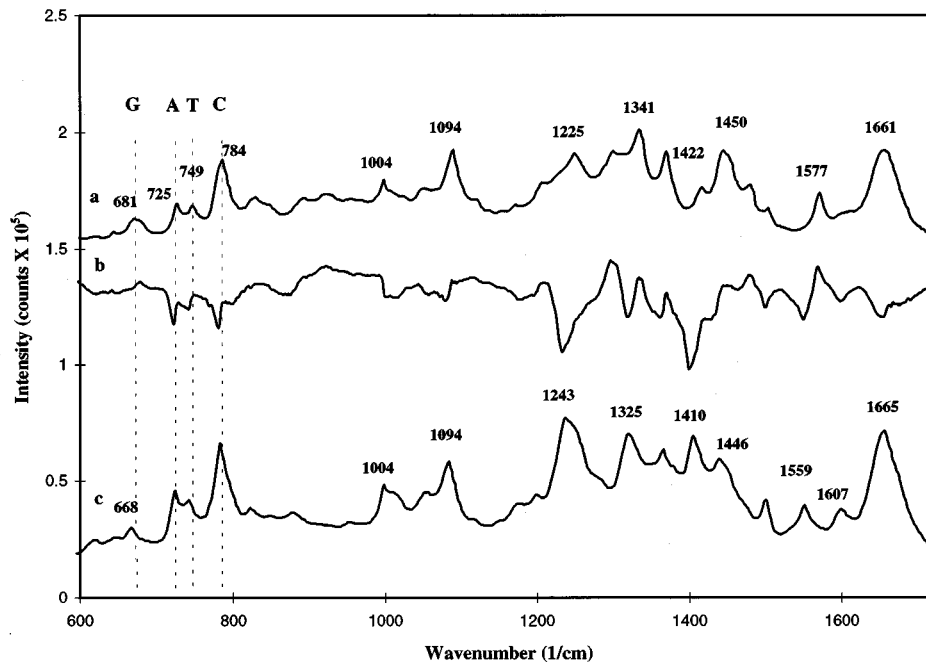
Fig. 18 Raman spectra of polytene chromosomes at (a) neutral pH and (b) pH of 1.8. (c) Difference spectrum of (a) and (b). Decrease in 681 cm^{-1} guanine peak and increase in the 725, 749, and 784 cm^{-1} peaks due to adenine, thymine, and cytosine, respectively, reflect base destacking with a drop in pH. The peak at 1448 cm^{-1}, which occurs at low pH, reflects protein extraction. (Modified from Ref. 44.)

Typically, 20–30 mW of excitation power is focused onto a small sample volume. Although no spectral degradation has been reported for pure DNA in solution under these conditions, dramatically different results are obtained when DNA in isolated chromosomes or in cells is examined under similar conditions.[45] Puppels and co-workers explored Raman spectra at 458, 488, 514, 632.8, and 660 nm excitation of calf thymus DNA, histone protein, isolated chromosomes and DNA in single human lymphocytes using a confocal Raman microspectrometer.[45] Excitation intensities of 0.5 to 20 mW were focused to a small spot, yielding a fluence of 5 MW/cm^2 for 10 mW irradiation. They observed

degradation of Raman spectra from isolated chromosomes and single cells at 458, 488, and 514 nm excitation, but not at 632.8 and 660 nm excitation. The damage manifests itself as a paling at the laser focus and a decrease in the Raman intensity, as well as a change in the relative intensity of some peaks.

Table 5 Changes in chromosomal DNA–protein ratio induced by pH treatment. (Modified from Ref. 44.)

Treatment	DNA-Protein	
	absolute (±19%)	normalized (±9%)
no	0.7	1
pH 3.6	0.7	1
pH 2.6	0.8	1.1
pH 2.2	0.9	1.3
pH 1.8	1.3	1.8
45% acetic acid	1.7	2.3

Table 6 Structural DNA changes in polytene chromosomes caused by pH treatment. (Modified from Ref. 44.)

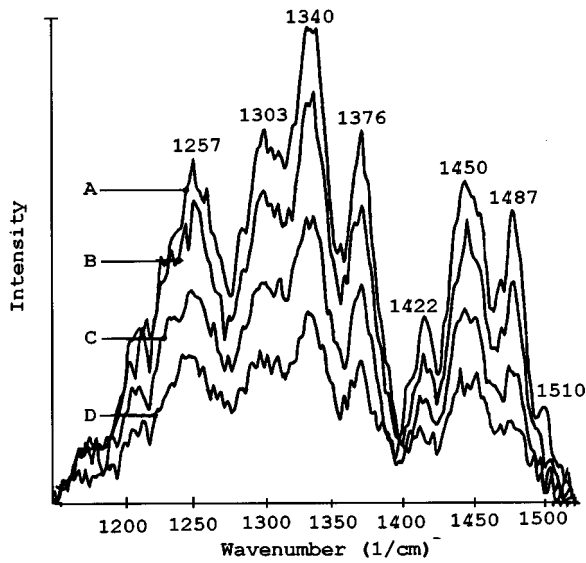| Spectral Change (cm^{-1})	Compositional or structural change
732 ↑	A, unstacking
800 ↑	BDA:BK
875 ↑	DNA:BK denaturation
900-1000↓	protein extraction
1017↑	DNA:BK
1144↑	DNA:BK
1185↑	T, unstacking
1239↑	T, unstacking
1300-1340↓	protein extraction
1450 ↓	protein extraction
1655 ↓	protein extraction
1670 ↑ (sh),	T, unstacking

Fig. 19 Raman spectra of a single metaphase chromosome exposed to 5 mW of 514.5 nm laser power focused on a 0.5 μm spot for (a) 1 min, (b) 3 min, (c) 5 min, and (d) 9 min. As the exposure times increase, the Raman signal decreases. The shape of the Raman spectrum changes with increasing exposure. (Modified from Ref. 45.)

Figure 19 illustrates the decrease in Raman intensity shown for successive intervals of irradiation with 5 mW of 514 nm light. In contrast, no changes were observed for 600 s of irradiation with 10 mW of 660 nm light. Raman spectra of pure DNA and histone protein, two of the major components which contribute to the Raman spectra of chromosomes and cells, were not affected under any of these conditions. Puppels excluded multiphoton processes, sample heating, and substrate heating as possible mechanisms which cause these changes. They speculate that the process is a photochemical reaction mediated by an unidentified sensitizer molecule that is present in cells and chromosomes, but not DNA and histone protein, and which absorbs at 514 but not at 660 nm.

Raman spectroscopy has been used to study the structure of DNA and its interactions with protein in chromosomes in human cells. Puppels et al. measured the Raman spectra from the nuclei of human granulocytes using a confocal Raman microspectrofluorimeter.[46] Using 6 mW of 660 nm excitation, spectra with good S/N ratios could be obtained with 150 s of integration. Spectra from the nuclei of eosinophils, basophils, and neutrophils showed little variability; Figure 20 shows a typical spectrum from the nucleus of a neutrophil. Spectral contributions from both DNA and proteins are identified; RNA and phospholipid contributions are absent. Using the ratio of the B DNA backbone vibration at 1094 cm^{-1} to the 1449 cm^{-1} protein vibration, which is relatively insensitive to secondary structure, they estimated the ratio of DNA to protein to be 1:2.3. A comparison of the spectra measured from the granulocyte nuclei with the sum of spectra from pure calf thymus DNA and pure calf thymus histone protein indicated that there are major contribu-
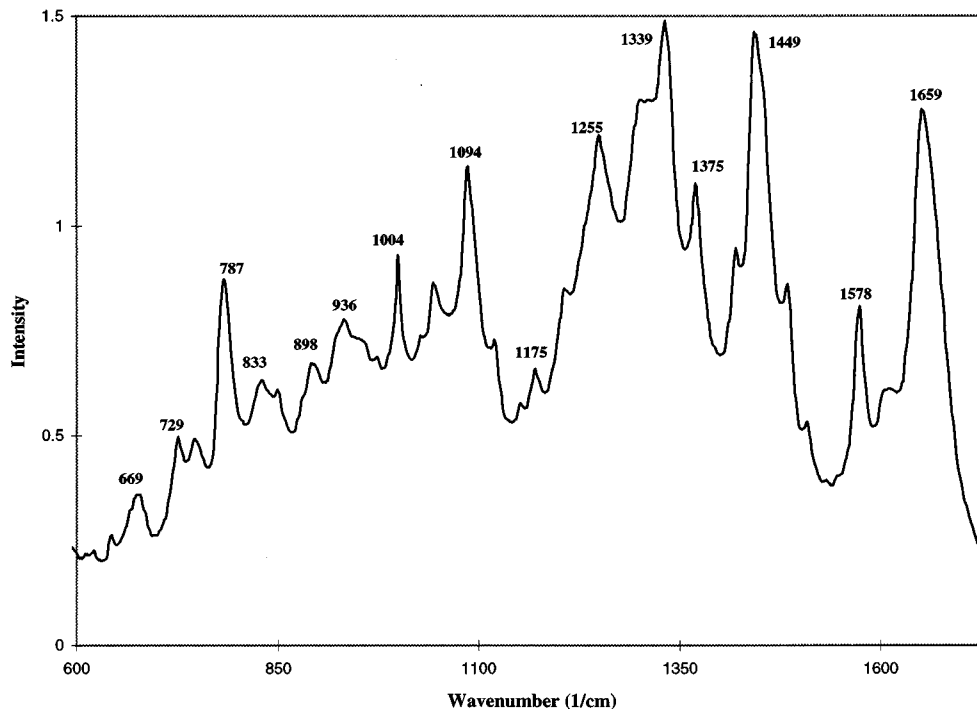

Fig. 20 Raman spectrum of the nucleus of intact neutrophilic granulocytes (660 nm, 6 mW, 150 s). (Modified from Ref. 46.)

tions from nonhistone proteins. The ratio of histone to nonhistone protein was estimated to be 1:1.3. Information about the secondary structure of nuclear protein and DNA was derived from the various peak positions and intensities. The predominant contributor to the spectrum was B form DNA. The spectra were complex enough so that other forms, which are expected to make up 5–10% of the DNA, were hard to detect. The authors suggest that if spectra from different regions of the nucleus containing predominantly one form of DNA can be measured, the difference spectra may enable detection of these other forms. The intensity from the DNA bases was lower relative to the backbone vibration at 1094 cm^{-1} than has been previously measured for DNA in solution at argon excitation. The authors attribute this to a wavelength dependence of the inelastic scattering spectra of DNA bases, rather than DNA–protein interaction. The proteins were found to be predominantly in the α-helix and random coil conformations.

4.3 MEMBRANES

In addition to protein and nucleic acids, Raman spectroscopy can also be used to study biological membranes. Verma and Sonwalker have shown that Raman spectroscopy can be used to study changes in cell membranes induced by γ irradiation.[47] Verma measured 514.5 nm excited Raman spectra of plasma membranes of V79 cells before and after γ irradiation and noted an altered protein secondary structure, an altered aromatic amino acid environment and changes in the thermal transitions of the lipid protein bilayer. The thermal transitions of the protein–lipid membrane were assessed from Raman spectra in the region of 2800 to 2950 cm^{-1}. Lipid peaks at 2850 and 2890 cm^{-1}, due to the symmetric and antisymmetric CH stretch in ethylene groups, were used to monitor thermal changes in lipids. The 2850 cm^{-1} peak is constant with temperature, but that at 2890 cm^{-1} is temperature sensitive and sensitive to interchain interactions, shifting to 2880 as the lipid matrix becomes a gel. Protein transitions were assessed by the intensity of Raman scattering at 2935 cm^{-1}, due to the temperature-sensitive symmetric C—H stretch in methyl groups. In addition, the protein secondary structure, as assessed from the amide I peak, showed a decrease in the total β strand and an increase in the total helix conformation. Verma concluded that changes in protein structure cause the proteins in irradiated cells to react differently with the lipids, altering the thermal transition properties of the membrane.

Thus, while Raman spectroscopy is a powerful tool for studying single biological molecules in solution, it can also be used to probe these molecules and their interactions in more complex biological systems. As a result, there has recently been much interest in using Raman spectroscopy to characterize and study normal, precancerous, and cancerous tissues.

5 RAMAN SPECTRA OF NORMAL AND NEOPLASTIC TISSUES

Raman spectra have been measured from intact tissues; however, collection and interpretation of tissue spectra have proven to be more challenging because of the strong fluorescence of the tissue chromophores and the complex mixture of biological molecules. Because high S/N Raman spectra, free of fluorescence, are so difficult to obtain, we first briefly review the instrumentation used to measure Raman spectra in tissue and then the tools that have been developed to separate Raman signals from the background fluorescence.

5.1 INSTRUMENTATION CONSIDERATIONS

Despite the wealth of information provided by Raman spectroscopy about the structure of biological molecules, early attempts to measure Raman spectra of tissues were limited by two factors: (1) the highly fluorescent nature of these samples and (2) instrument limitations, which necessitated long integration times and high power densities to achieve spectra with good signal-to-noise ratios. The initial Raman spectra of tissue were measured with visible laser excitation, using primarily the argon laser lines (see, for example, Refs. 48 and 49). With the development of interferometers, Fourier transform Raman spectroscopy was used to measure tissue Raman spectra, typically using 1064 nm (Nd:YAG) for excitation with germanium detectors.[5,6] FT-IR Raman spectroscopy uses preresonance excitation to reduce the fluorescence contribution and thus allows the measurement of Raman spectra even on highly fluorescent samples with little or no fluorescence, and yields spectra more detailed than those obtained using visible excitation (Fig. 21).[5] This technique yielded acceptable S/N with moderately high power densities, but collection times on the order of 30 min were required to obtain spectra of highly fluorescent, scattering tissues such as human arteries.[50] More recently, the development of diode lasers and cooled silicon CCD cameras sensitive in the near-IR has enabled the measurement of tissue Raman spectra with NIR excitation. Diode lasers can provide excitation typically in the region of 750–850 nm, which allows the use of silicon detectors (sensitive only to 1100 nm). The advantage of this technique is that fluorescence emission is reduced and spectra with acceptable S/N ratios can be achieved with relatively short integration times (<1 min).[51]

5.1.1 Fluorescence Elimination

Even with NIR and IR excitation, some residual fluorescence is detected, and accurate subtraction of this signal to yield the vibrational spectrum continues to present a significant challenge since the fluo-
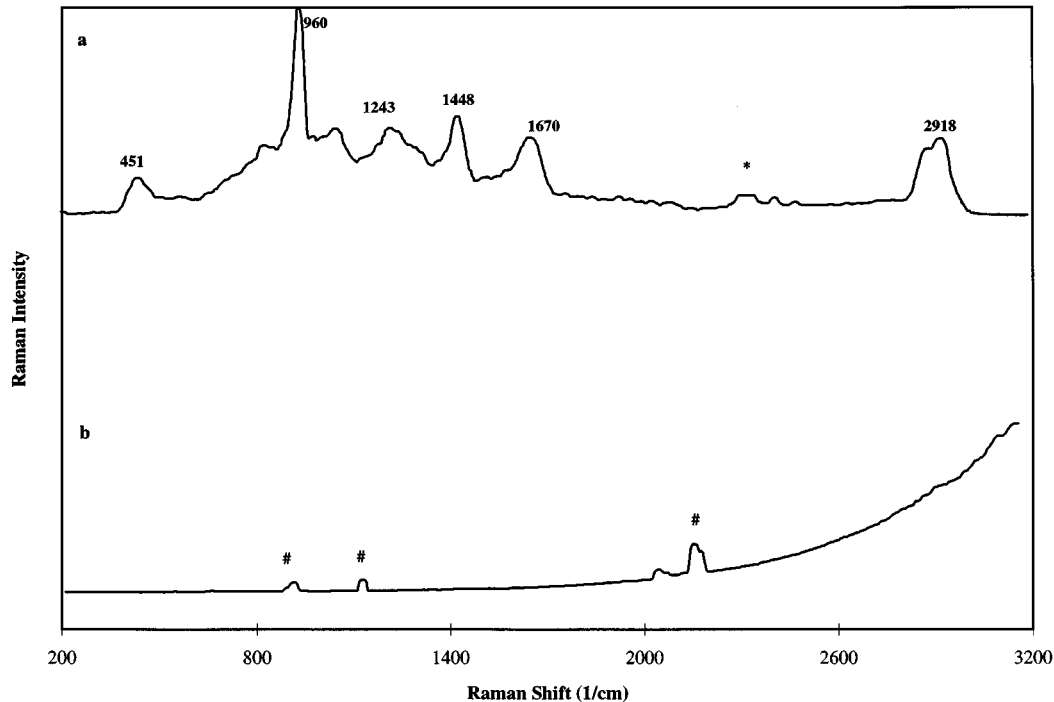
Fig. 21 Comparison of (a) FT Raman spectrum at 1064 nm excitation (300 scans, 1.0 W) and (b) visible excited Raman spectrum at 647.1 nm excitation (10 mW, 1 s) from a chicken leg bone. # indicates plasma lines. * indicates an artifact. (Modified from Ref. 5.)

rescence and Raman signals lie in the same spectral range. In biological samples, the fluorescence background is due to the intrinsic tissue autofluorescence, which is difficult to eliminate without altering sample composition. Even though the quantum yield of this signal may be as low as 10^{-4} (for example, reduced nicotinamide adenine dinucleotide, NADH),[52] tissue autofluorescence can be substantially more intense than the inelastic scattering of tissue.[50] This led to the development of different techniques to effectively separate the Raman signal from a measured tissue spectrum.

Several experimental as well as mathematical tools have been proposed to separate the contribution of fluorescence to yield the intrinsic Raman scattering. A simple approach to prevent fluorescence interference could be the addition of a fluorescence quencher;[53] however, this requires a quencher that is itself not Raman active. A more feasible technique involves gating out the fluorescence by selecting a suitable detector gate.[54] This technique takes advantage of the short lifetimes of Raman scattering events ($\approx 10^{-11}$ to 10^{-13} s) compared with fluorescence lifetimes ($\approx 10^{-9}$ to 10^{-7} s) in biological samples to temporally differentiate between Raman and fluorescence signals.[55] Using a pulsed laser source, a time gate can be used to synchronize the detector with the laser pulse so that all the Raman signal is collected, while a large fraction of the fluorescence is rejected. The measured spectrum can also be polarization modulated, taking ad-

vantage of the polarizability of Raman scattering to eliminate fluorescence that is unpolarized.[56]

Illuminating samples with frequency-modulated excitation light can be used in different ways to reject fluorescence. The wavelength of the excitation light is modulated at low frequencies (a 60-Hz modulation frequency with 0.5-nm shifts at argon excitation) to reject fluorescence. Since fluorescence is independent of the excitation wavelength, modulation yields a time-invariant fluorescence signal. On the other hand, Raman scattering frequencies shift with the modulated excitation light. If lock-in detection is used at the modulation frequency, the detected signal can be regarded as the derivative of the Raman signal (with respect to wavelength) free of fluorescence.[57] Although this technique is an effective one, it requires the use of specialized instrumentation for modulation and lock-in detection. This concept can be simply applied by measuring the spectra at two slightly shifted excitation wavelengths and taking their difference [Figs. 22(a) and 22(b)].[50,58] Again, the fluorescence remains unchanged at both excitation wavelengths whereas the Raman peaks are shifted. The difference of the two spectra is comparable to the first derivative of the Raman spectrum; integrating the difference spectrum yields the original Raman signal [Fig. 22(c)]. A similar result can be obtained by measuring the spectrum at any excitation wavelength and taking the first derivative of the spectrum [Fig. 23(c)]. The Raman spectrum can be obtained by in-
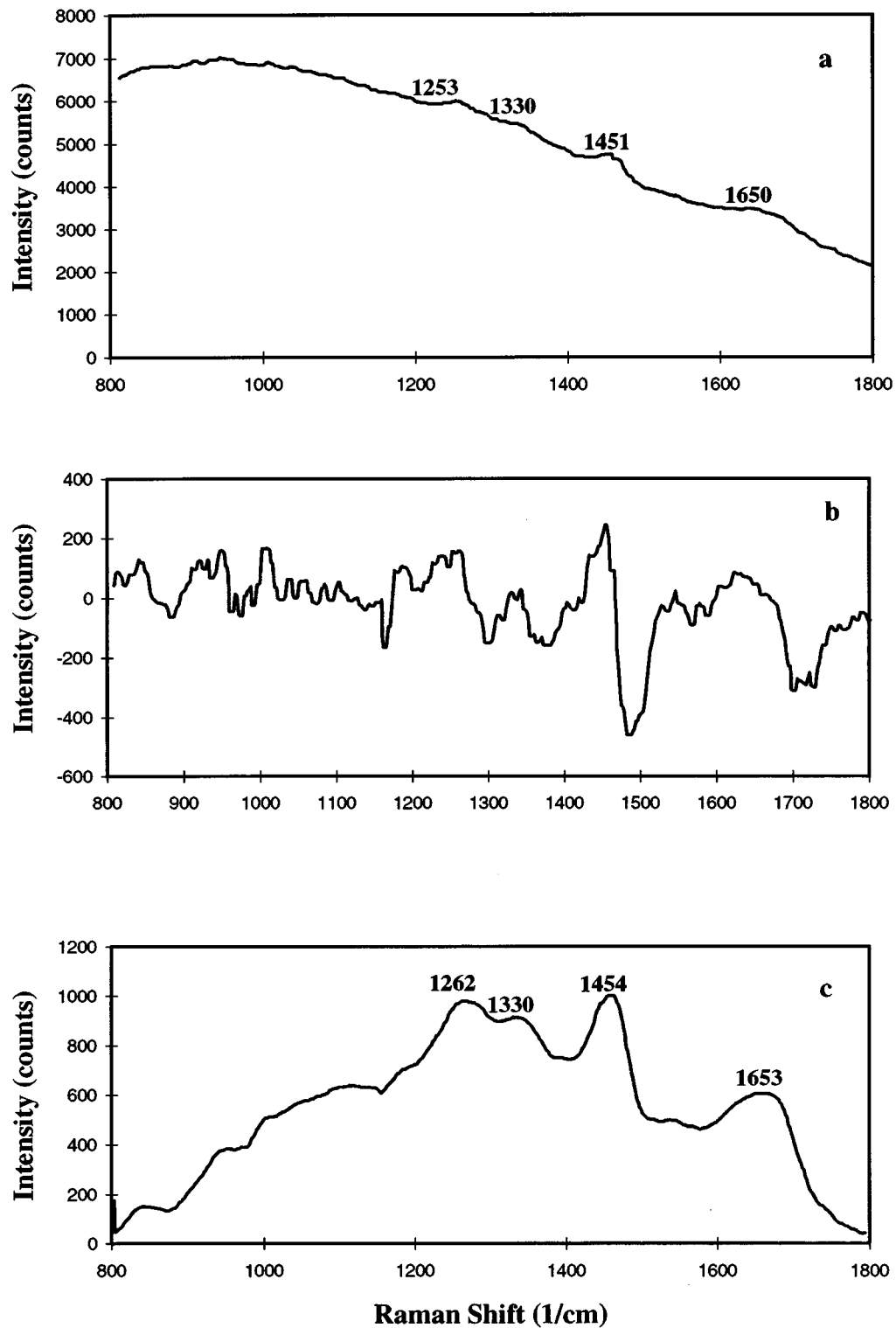
Fig. 22 Raman spectra of normal human aorta, intimal side: (a) spectrum measured at 810 nm excitation (20 mW, 5 min), (b) difference spectrum of Raman spectra excited at 810 and 812 nm, and (c) fluorescence-subtracted Raman spectrum obtained from integrating (b). (Modified from Ref. 50.)
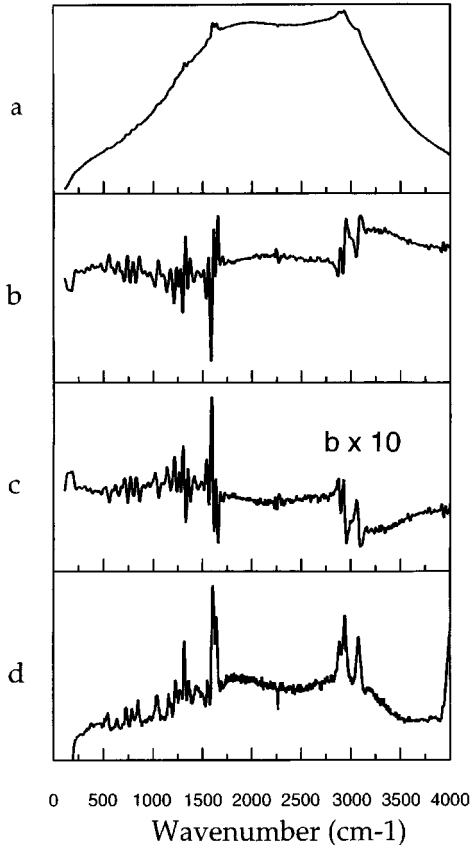
nique, the measured spectrum is noise-smoothed and then Fourier transformed to the frequency domain by taking the FFT of the signal. The FFT signal is multiplied with a linear digital filter to eliminate the fluorescence [Fig. 23(d)]. The inverse FFT then yields the Raman spectrum, free of fluorescence.[55] Figure 23 is a comparison of the shifted excitation, first derivative, and FFT techniques used to extract the Raman signal from the same sample.

Another simple and accurate method to subtract fluorescence is to fit the spectrum containing both Raman and fluorescence information to a polynomial of a high enough order to describe the fluorescence line shape but not the higher frequency Raman line shape.[25] A fifth-degree polynomial was found to be optimal by Mahadevan et al.[25] The best fit polynomial was then subtracted from the spectrum to yield the Raman signal alone (Fig. 24).

Each of the different techniques has advantages and disadvantages and the selection of method should be based on the specific application and measurement technique used (Table 7). Mosier-Boss, Liebermen, and Newberry tested the use of the shifted excitation, first derivative, and FFT techniques for fluorescence subtraction, and a preference for using the FFT was indicated due to its ability to filter out random noise from the spectrum.[55] Mahadevan et al. used some of the above techniques with cervical precancers and found the use of a polynomial fit to be the simplest technique, from experimental as well as computational points of view, which still yielded accurate results.[25]

Fig. 23 Raman spectra of a pain-relief drug: (a) spectrum at 488 nm excitation (50 mW, 10 sec), (b) smoothed difference spectrum obtained from two Raman spectra shifted by 10 cm^{-1} with respect to each other, (c) taking the first derivative of smoothed Raman spectrum from (a) and (d) spectrum obtain from performing FFT of (a), multiplying with a highpass linear filter and then performing an inverse FFT. (Modified from Ref. 55.)

tegrating the noise-smoothed derivative spectrum following baseline correction.[55] Another mathematical tool that can be used for fluorescence subtraction is the fast Fourier transform (FFT). In this tech-

5.2 EFFECT OF SAMPLE CONDITIONS

Although many groups have suggested that Raman spectra could be useful for *in vivo* tissue analysis, the instrument limitations described above have forced most studies to be conducted *in vitro* to as-
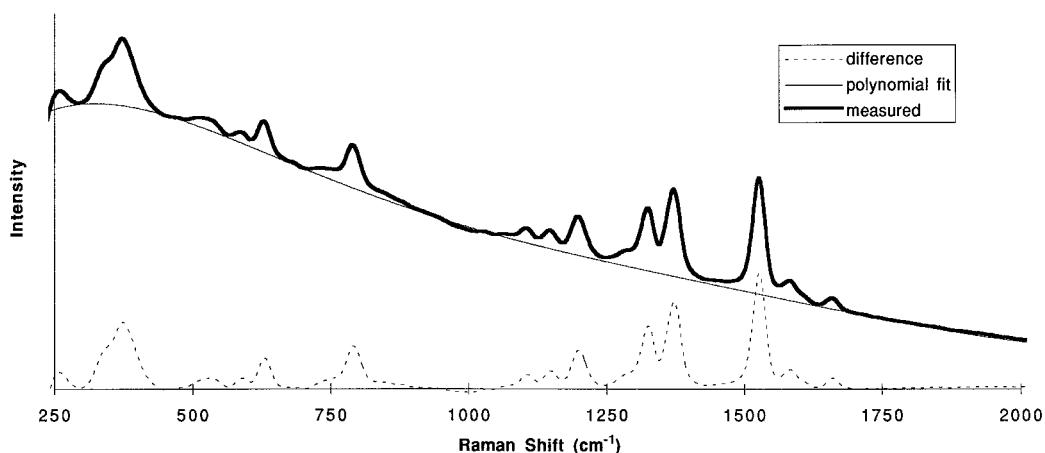

Fig. 24 Raman spectra of rhodamine 6G. Solid thick line indicates spectrum as measured at 789 nm excitation (25 mW, 20 s). Solid thin line indicates the fifth-order polynomial fit of spectrum. Dashed line indicates the fluorescence-subtracted Raman spectrum. (Modified from Ref. 25.)

Table 7 Comparison of different techniques for correction of fluorescence background from measured Raman signal.

Technique	λ_{exc} Modulation	Shifted λ_{exc}	1st Derivative	FFT	Polynomial Fit
Description	Raman signals follows λ_{exc}, fluorescence is invariant	Raman signals shifts with λ_{exc}, fluorescence is invariant	Edge detection-take first derivative, shift baseline, integrate	Signal is Fourier transformed, highpass filtered & inverse transformed	Broadband signal is fit to a high order polynomial
Advantages		No special instruments needed, allows use of multichannel detection	No special instruments needed, no change in λ_{exc} needed	Can discard random noise	Computationally simple
Disadvantages	Need for modulator, lock-in detector, baseline, and baseline drift problems	Baseline and baseline drift problems	Finding appropriate baseline for fluorescence subtraction, problem with baseline drifts	Computationally expensive, choice of filter critical	Negative errors in fit, multiple fluorescence peaks may be difficult

sess the feasibility of clinical application. To biologically simulate *in vivo* conditions, most studies have been conducted with extracted tissues that have been frozen (with liquid nitrogen or dry ice) at the time of collection and thawed for study or fixed in formalin to prevent deterioration. To determine whether spectra recorded from tissues preserved by freezing or formalin fixation yield useful information for *in vivo* application, studies have been conducted *in vitro* to compare spectra of freshly excised and preserved tissues and later *in vivo* on animal tissue.

5.2.1 Fixed Versus Fresh Tissues

Several groups have studied the effect of fixation on tissue Raman spectra obtained *in vitro*.[59–61] Fixation preserves the tissue by promptly interrupting its metabolism as well as stabilizing its structure. Formalin is one of the most commonly used fixatives and it accomplishes its goal by promoting the cross-linkage of amine groups in tissue proteins.[62] When fresh and formalin-fixed rabbit liver tissues were compared *in vitro* using FT Raman spectroscopy, the most significant difference was found to be the strength of the Raman band at 1593 cm^{-1}, which is the most prominent band in the spectrum of biliverdin (Fig. 25).[61] Fixed liver kept in formalin for several days shows a progressive decrease in the biliverdin band compared with fresh tissue. This is consistent with the physiology of liver, in which abundant bilirubin, an end product of hemoglobin decomposition, may be found and is oxidized to biliverdin.[28] In another study, fresh and fixed rabbit eye lenses were compared using Raman microspectroscopy.[59] The lenses were fixed using a cacodylate-buffered paraformaldehyde solution. Prior to study, the fixative was drained and the lenses washed. The Raman spectra of fresh and fixed lenses were found to be similar. No peaks or shoulders from the Raman spectrum of the fixative were found. In fact, the water-to-protein ratio was found to be similar in fresh and fixed tissue, indi-

cating minimal influence from fixation. In another study assessing the use of visibly excited Raman spectra for detection of breast cancer, fresh and formalin-fixed breast tissue samples were compared.[60] A small increase in the intensity of lipid bands relative to carotenoid bands was observed in fresh tissue. Again, no additional peaks or shoulders were observed in the Raman spectra of fixed breast tissue.

These studies indicate that, although some differences are observed in the Raman spectra of fresh and fixed tissues, the variation appears to be small and does not affect the potential diagnostic capability of the spectrum. Thus, until reliable instruments are available for *in vivo* studies, it appears that the study of fixed specimens yields useful results as long as one is aware of the possible implications. This is in contrast to fluorescence spectroscopy, where fixation can induce significant changes in the tissue fluorescence spectrum (unpublished data from R. Richards-Kortum, A. Mahadevan, and N. Ramanujam, 1994).

5.2.2 Animal Versus Human Tissues

Another way to address the difficulty of recording Raman spectra from human tissue *in vivo* is to use animal tissues that resemble human tissues in function and structure to simulate the behavior of human tissues. However, Raman spectra of animal tissues can in some cases differ from those of human tissues, resulting in conclusions not valid for humans. One example of this is the use of mouse eye lenses to study the aging of lenses.[63] In early studies, Yu suggested that the intensity of Raman bands at 2580 cm^{-1} due to sulfhydryl groups (—SH) and 508 cm^{-1} due to disulfide groups (—S—S) can be used to calculate their relative concentrations, which can then be related to aging and cataract formation.[63] In an extensive study of mouse lenses, a fall in —SH concentration and a corresponding
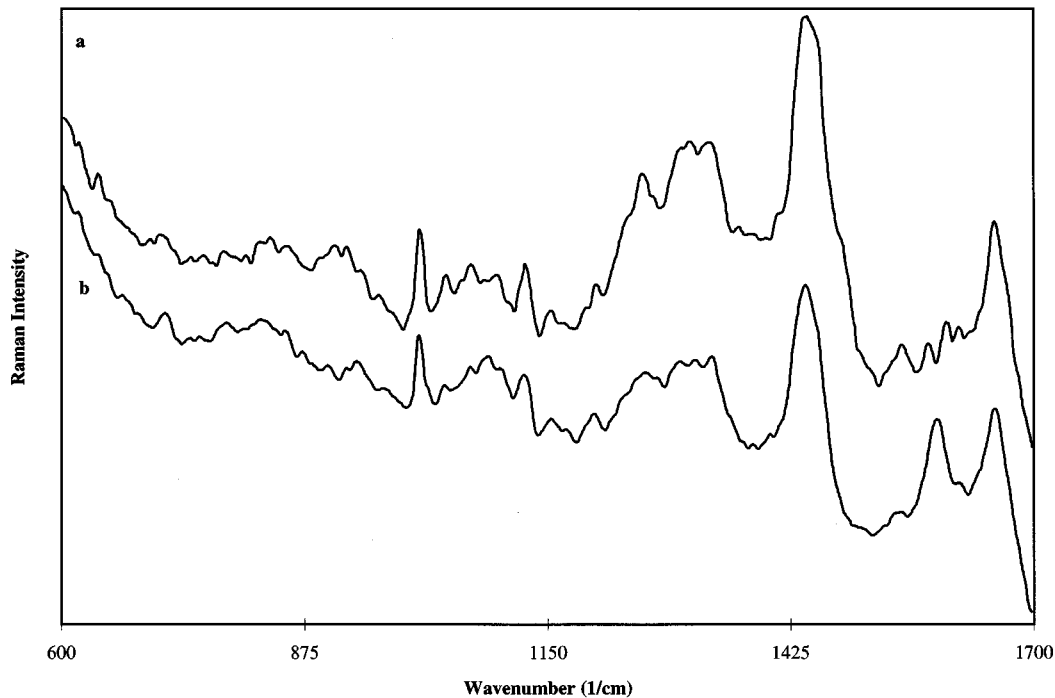
Fig. 25 FT Raman spectra of rabbit liver at 1064 nm excitation (250 mW, 150 min): (a) spectrum of rabbit liver fixed in formalin for 14 days and (b) spectrum of fresh rabbit liver. (Modified from Ref. 61.)

increase in —S—S concentration was observed along the visual axis of mouse lens nucleus from 1 to 6 months. A tandem increase in protein development with a decrease in sulfhydryl was concluded to accompany the normal aging process. However, on repeating these studies on guinea pig and human lenses, a different phenomenon was observed. Figure 26(a) compares the spectra of mouse and guinea pig lenses and shows the differences in the 508 cm^{-1} band. Although guinea pig lenses also showed a decrease in sulfhydryl intensity, no corresponding increase in disulfide band was observed. Human eye lenses were similar to guinea pig lenses. This study clearly indicates the pitfalls in improper selection of an animal model and indicates that independent verification of the model is needed to ensure that results will be applicable to human conditions.

Other groups have compared the feasibility of using animal models for different organ sites. For the study of transdermal drug infusion, the use of snake or pig skin as an animal model for human skin was considered.[64] The FT Raman spectra from these three types of skin were compared with respect to differences observed with drug delivery. Although pig skin resembles that of humans more closely, the ease of availability of snake skin due to molting makes it a popular model. The FT Raman spectra from the three tissues show remarkable similarities in their characteristics despite significant differences in their environment and function

[Fig. 26(b)]. The spectra indicate that the tissues contain similar components but differ slightly in their states and quantities. These differences manifest themselves in slight changes in intensities, locations, and shapes of the corresponding spectra. For example, the lipid bands at 2931 and 2883 cm^{-1} are similar for human and pig skin, varying primarily in intensity. However, the presence of an additional band at 2975 cm^{-1} in snake skin indicates that its lipid content and conformation differ from the mammalian skins. Other spectral differences can also be observed. The differences between pig and human skin are negligible compared with snake skin, making pig skin a more suitable animal model.

5.2.3 *In Vitro* versus *In Vivo* Tissues

Studies indicate that fixation can be a viable method of preserving extracted tissue for Raman spectroscopy. A primary concern in devising a clinical diagnostic system based on Raman spectroscopy is whether the spectra of excised tissue resemble those of tissue spectra acquired *in vivo* and whether the information obtained from these *in vitro* studies can be applied to a clinical setting. Spectra from intact human stratum corneum were compared with those from excised human stratum corneum.[65] Significant differences in the Raman spectral features were observed (Fig. 27). Increased intensity of the C—C stretching vibrational bands at 1030 and
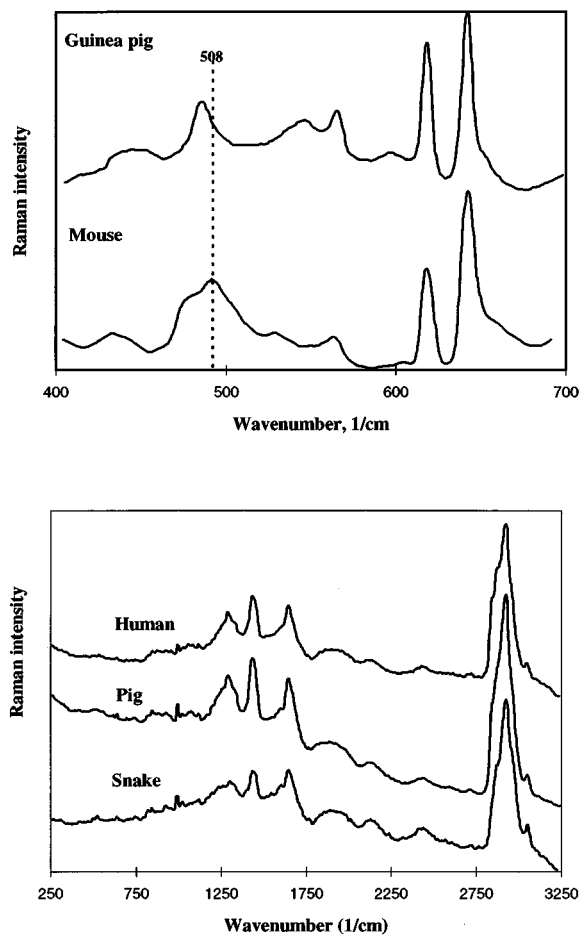
Fig. 26 Raman spectra from eye lens and skin to indicate the need for careful selection of animal model, (a) Raman spectra of mouse and guinea pig lens at 514.5 nm excitation (150 mW, 5 min). (Modified from Ref. 63.) (b) FT Raman spectra of stratum corneum from human, pig, and snake skin at 1064 nm excitation (250 mW, 200 scans). (Modified from Ref. 65.)

1130 cm^{-1} were observed *in vivo*. An additional spectral band at 3230 cm^{-1} of unknown origin is observed only *in vivo*. Thus, it is important to be aware of the potential differences that may occur when moving from *in vitro* studies in *in vivo* conditions.

Another important consideration when extrapolating the results obtained *in vitro* for *in vivo* conditions is the physical dimension of the sample to be studied *in vitro* relative to the excitation wavelength. In one study, FT Raman spectra collected from a fingernail *in vivo* were compared with a cut nail.[6] Intact nail spectra show features from the underlying nail bed in addition to the nail characteristics, clearly indicating the increase in sample volume that was probed *in vivo*. To study the effect of sample dimension on the propagation of light, Monte Carlo simulations were performed assuming a heterogeneous sample to obtain a relation between sample dimensions and geometry and the emitted signal.[66] Although these simulations were

performed for elastic scattering and fluorescence, a similar dependence on sample size can be expected for inelastic scattering as well. The results indicate that signal reaching the front surface of a tissue cube is a strong function of the cube volume relative to the tissue optical properties. Thus if *in vitro* measurements from multiple biopsy specimens are to be compared, each sample should have the same physical dimensions. A cube with dimensions greater than about 125 optical depths at the excitation wavelength approaches a semi-infinite tissue geometry for the optical properties simulated, i.e., signal is emitted primarily from the top surface. If *in vitro* measurements are to be extrapolated to an *in vivo* tissue geometry, the biopsy specimens should be large enough so that no signal escapes from the sample bottom and side boundaries.

Figure 28 shows that for the optical properties of aortic intima (λ_{exc}=476 nm, μ_a=7.5 cm^{-1}, μ_s=240 cm^{-1}, g=0.85), a 1 cm cube meets these criteria. The percent of excitation light absorbed and the percent of generated signal reabsorbed and remitted from the sides and bottom change rapidly as the cube dimension increases from 0.4 mm to 4 mm in the aorta. Figure 28 also suggests that when only small *in vitro* samples are available, the sample dimension should be at least 75 to 100 optical depths (25 to 35 mm for arterial tissue at 800-nm excitation) for results to more closely resemble those expected from intact tissue. Below this limit, the amount of signal remitted, as well as its line shape, will be a strong function of the tissue dimension.

6 CANCERS AND PRECANCERS IN TISSUES

The preceding sections of this paper have provided an overview of Raman signals from biological molecules in solution and in microscopic environments. Several biological molecules such as nucleic acids, proteins, and lipids have distinctive Raman features that yield structural and environmental information. The molecular and cellular changes that occur with cancer may result in distinct Raman spectra from normal and cancerous tissues. The transitional changes in precancerous tissues as well as in benign abnormalities such as inflammation could also yield characteristic Raman features that allow their differentiation. For example, one of the more prominent changes that occurs with cancers and precancers is increased cellular nucleic acid content; extensive DNA studies indicate that it may be possible to sample this change using Raman spectroscopy.[61,67] In recent years, several groups have indicated the potential of vibrational spectroscopy for cancer diagnosis in various organ sites. These groups have shown that features of the vibrational spectrum can be related to molecular and structural changes associated with neoplastic transformation. Raman spectroscopy has thus far been used to de-
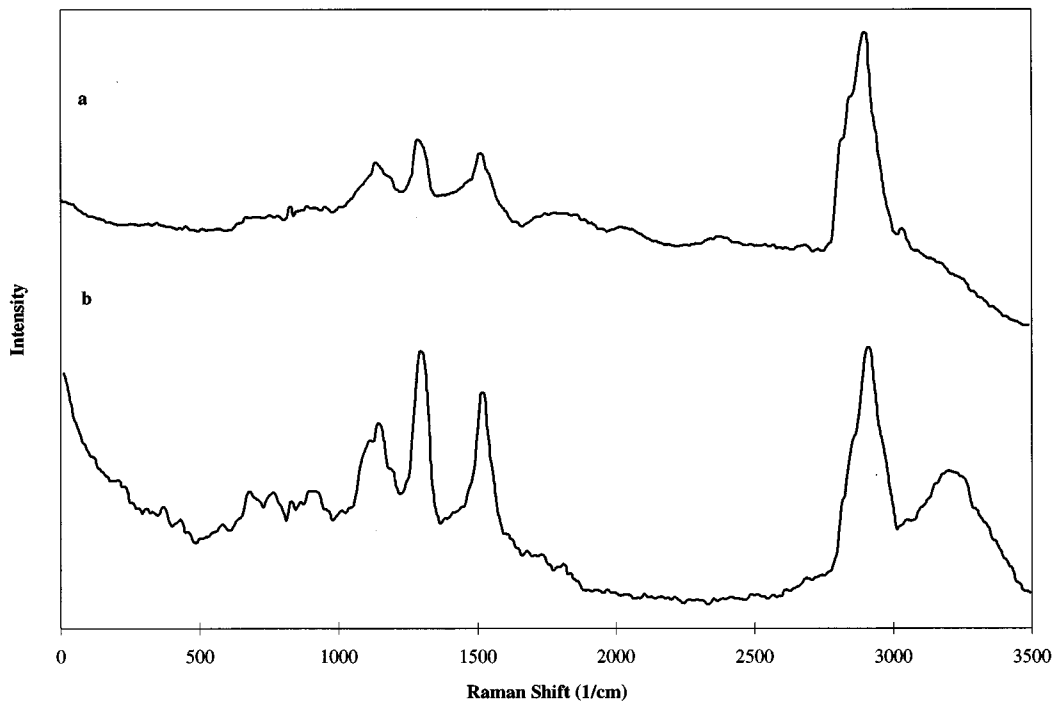
Fig. 27 FT Raman spectrum of human stratum corneum at 1064 nm excitation (a) *in vitro* collection (350 mW, 200 scans) and (b) *in vivo* collection (300 mW, 500 scans). (Modified from Ref. 65.)
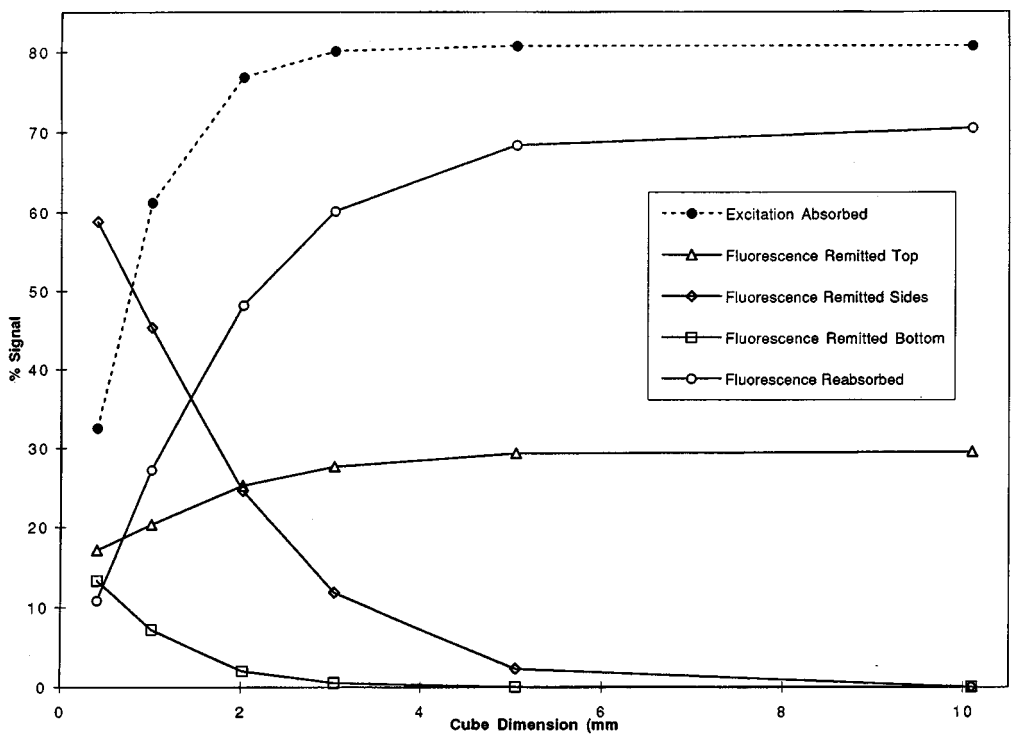

Fig. 28 Percent signal emitted as a function of cube volume using aortic intima as an example. (Modified from Ref. 66.)

tect cancers of epithelial and mesenchymal origin, such as breast, brain, colon, bladder, and gynecologic tissues.

6.1 BRAIN AND OTHER SARCOMAS

The brain is one of the most complex organs in the human body, making it a very difficult target of study. In broad terms, brain substance is divided into gray matter consisting of nerve cells and white matter consisting of primarily myelinated nerve fibers or axons; myelin is a fatty substance that insulates the axons.[68] Neurons, glia, and the cells that form the meninges and blood vessels form the cellular components of the brain. Glia arise from the bone marrow and support the neurons. Glial cells include astrocytes, present in gray and white matter, which have round nuclei with even, pale chromatin. Gliomas are tumors that arise from glial cells and differ in their characteristics based on their origin cells. Neurinomas are derived from Schwann cells and are most commonly accompanied by hearing loss; hence they are called acoustic neurinomas. Neurocytomas are tumors that are characterized by round uniform nuclei that resemble those of glial oligodendrocytes but are neuronal in origin.[13]

Several groups have been responsible for the Raman study of human brain and some of its tumors (see, for example, Refs. 61 and 69). Mizuno et al. have extensively studied the FT-IR Raman spectra of different kinds of brain tumors relative to that of normal human brain tissue excised from human patients. In general, the spectra of normal white and gray matter of the brain show primary peaks due to lipids and proteins.[69] The spectra of white matter show a greater contribution from lipids, cholesterol, and proteins than the spectra of gray matter which show a greater contribution from water, as is consistent with normal brain structure [Figs. 29(a) & 29(b)].[61]

The spectra of different tumors were studied: glioma II and III (origin–astrocytes), neurinoma (origin—Schwann cells), and neurocytoma (origin—arachnoid choroid plexus).[69] FT Raman spectra of grade II gliomas were similar to that of gray matter. However, grade III gliomas showed several spectral differences relative to normal brain tissue [Fig. 30(a)]. A strong band was observed at 1245 cm^{-1}, indicating a change in protein configuration from α-helix to random coil. The intensity of the C—C lipid stretching band at 1130 cm^{-1} is increased. A band at 856 cm^{-1} due to polysaccharides is also observed. Neurinomas show spectral characteristics similar to that of gray matter except for bands at 956, 1006, 1157, and 1524 cm^{-1}, attributed to carotenoids that are absent in normal tissues [Fig. 30(b)]. Neurocytomas display a sharp band at 960 cm^{-1}, associated with hydroxyapatite [Fig. 30(c)]. These kind of tumors are often accompanied by calcification, as is indicated by the apatite band. Thus, each tumor type presents specific bands that can be
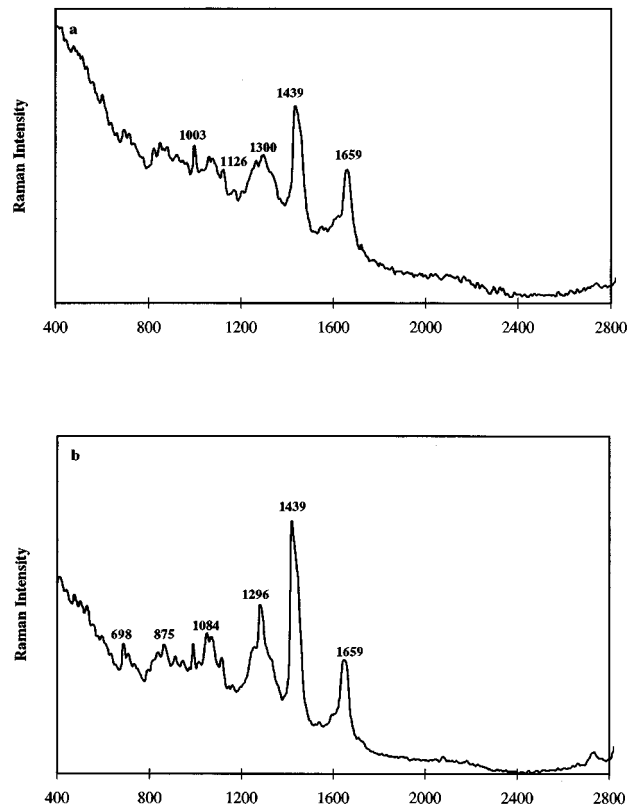

Fig. 29 FT Raman spectra of normal human brain tissue at 1064 nm excitation (200 to 300 mW, 1000 to 3000 scans): (a) normal gray matter and (b) normal white matter. (Modified from Ref. 69.)

used as potential diagnostic features (Table 8). Keller et al. also studied normal brain tissues and several neurogenic sarcomas grown in mice.[61] Spectral differences include a protein band at 1247 cm^{-1}, absence of the bands at 700 and 960 cm^{-1}, and additional bands due to nucleic acids in brain sarcomas. The protein band at 1247 cm^{-1} is more intense in normal brain and is attributed to a larger amount of protein, probably collagen. The bands at 700 and 960 cm^{-1}, due to cholesterol, are present in both normal gray and white matter but are absent in neurogenic sarcomas. Additional bands typical of nucleotides were also observed in sarcoma spectra, but were not detected in normal brain. However, in contrast, Mizuno et al. observed a more intense band at 1245 cm^{-1} in gliomas as described above. In addition, the band at 960 cm^{-1}, attributed to hydroxyapatite, was observed only in neurocytoma samples.

Manoharan et al. studied liposarcomas, a cancer of adipose tissues usually occurring in the extremities.[51] NIR Raman spectra were obtained from liposarcomas and normal adipose tissues (Fig. 31). The spectrum of normal tissues shows lipid bands due to C—H, C—C, C=C, and C—O vibrations. In addition to lipid bands, the spectrum of a
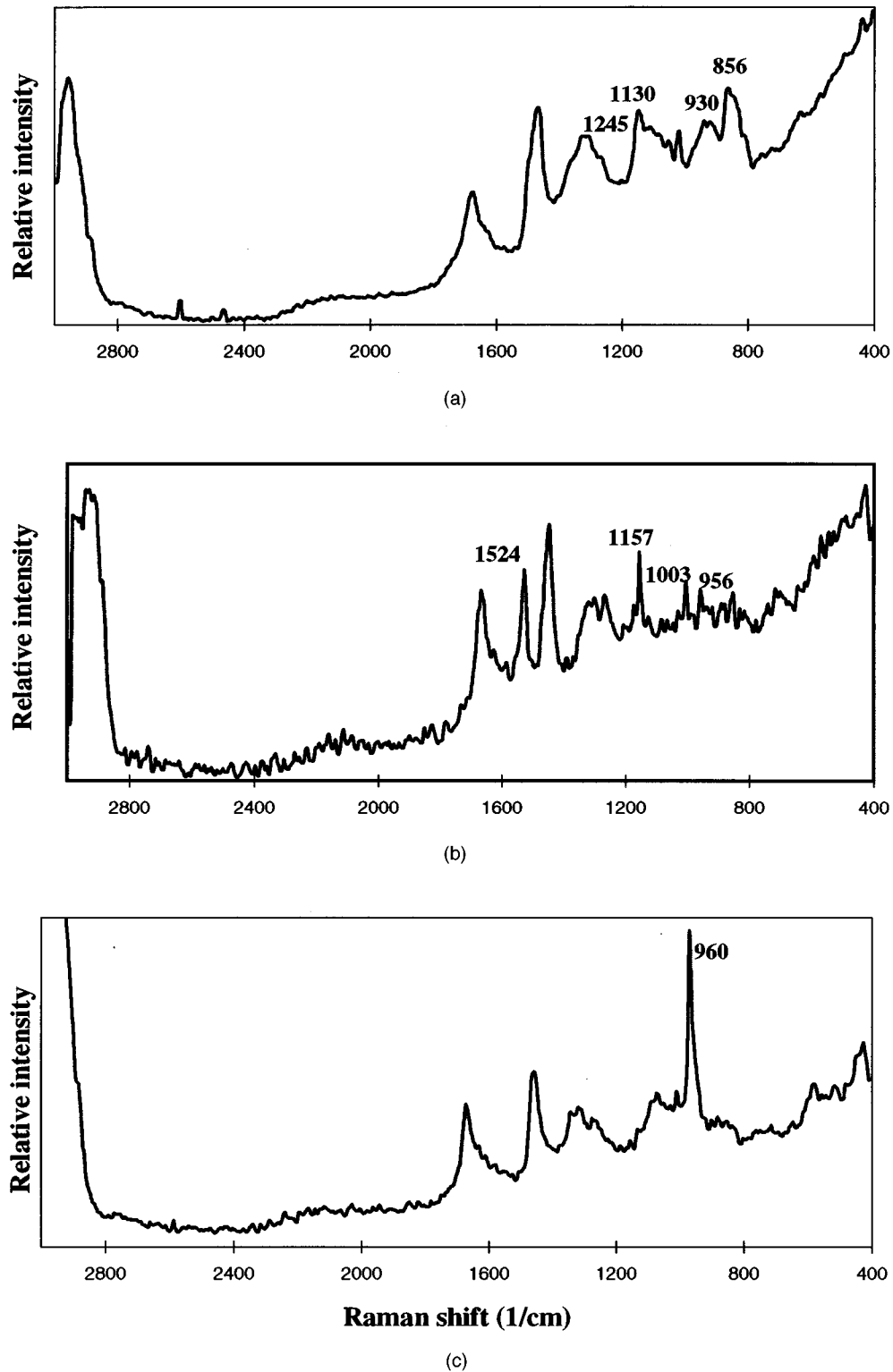
Fig. 30 FT Raman spectra of human brain tumors at 1064 nm excitation (200 to 300 mW, 1000 to 3000 scans): (a) glioma grade III, (b) acoustic neurinoma, and (c) central neurocytoma. (Modified from Ref. 69.)

liposarcoma shows cartenoid bands at 1528 and 1156 cm^{-1}. The intensity ratio of the CH_2 bending mode at 1442 cm^{-1} to the $C{=}C$ stretching band at 1667 cm^{-1} is observed to decrease with the grade of malignancy compared with normal tissue. Thus, these features can potentially be used as diagnostic parameters to identify malignant tumors and determine their grades.

Table 8 Summary of vibrational bands observed in normal brain and different brain tumors. (Adapted from results in Ref. 69.)

Gray & White Matter	Glioma III	Neurinoma	Neurocytoma	Bond Assignment	Molecular Assignment
852	856				polysaccharides
875					
883					
	930				
		956		carotenoids	carotenoids
			960	hydroxyapatite	hydroxyapatite
1003	1006	1003	1003	ring breathing	phenylalanine
1065	1068		1068	C—O, C—O—C stretch	phospholipid
1080				C—C, PO_2^- stretch	phospholipid
1126	1130			C—C stretch	phospholipid
		1157		carotenoids	carotenoids
	1245			amide III	proteins (random)
1269		1265	1272	amide III	proteins (α-helix)
1300	1304	1296	1315	CH_2 twist & wag	phospholipid
1439	1446	1439	1446	CH_2 deformation	lipids & proteins
	1524			carotenoids	carotenoids
1659	1659	1659	1659	amide I	amide proteins
2850				CH_2 stretch	lipid hydrocarbons
2885		2885		CH_2 stretch	lipid hydrocarbons
2931	2927	2930		CH_3 stretch	lipid hydrocarbons

6.2 BREAST CANCER

Perhaps the most extensive work on the use of Raman spectroscopy for cancer detection has been for breast cancers. This is the most common type of cancer among women, accounting for 18% of all cancer deaths among women, second only to lung cancer.[12] The breast consists of mammary glands arranged in lobes separated by fibrous connective tissue and a considerable amount of fatty tissue.[68] Fibrocystic changes are benign processes that vary from the innocuous to those associated with the risk of carcinomas and are primarily the result of hormonal imbalances. They may exist in three forms: cyst formation and fibrosis, hyperplasia, and adenosis. Breast tumors may arise from the epithelium, glands, or connective tissue and usually consist of fat, connective tissue, epithelium, and a protective covering. They vary from adenomas and adenocarcinomas to fibromas and fibrosarcomas. Infiltrating ductal carcinoma (IDC) is an invasive form of breast cancer studied using Raman spec-

troscopy. IDCs typically show an increase in dense fibrous stromal tissue and are fairly well defined masses with a hard consistency.[13] Although routine screening using mammography can aid in early detection of malignancy, lesions identified with this method must be biopsied and evaluated histopathologically to determine whether treatment is necessary. In recent years, attempts have been made to use spectroscopic techniques to diagnose breast cancer.[10,16,70] Although fluorescence spectroscopy has shown some promise as a diagnostic tool, Raman spectroscopy may provide more definitive characteristics that allow differentiation of benign and malignant tumors.[8]

Several groups have explored the potential of Raman spectroscopy for detecting breast cancer. Alfano et al. obtained FT-IR Raman spectra of excised normal human breast tissues, benign, and malignant breast tumors, and discussed the feasibility of using FT Raman spectroscopy for differentiating normal and malignant breast tissues.[70] The vibra-
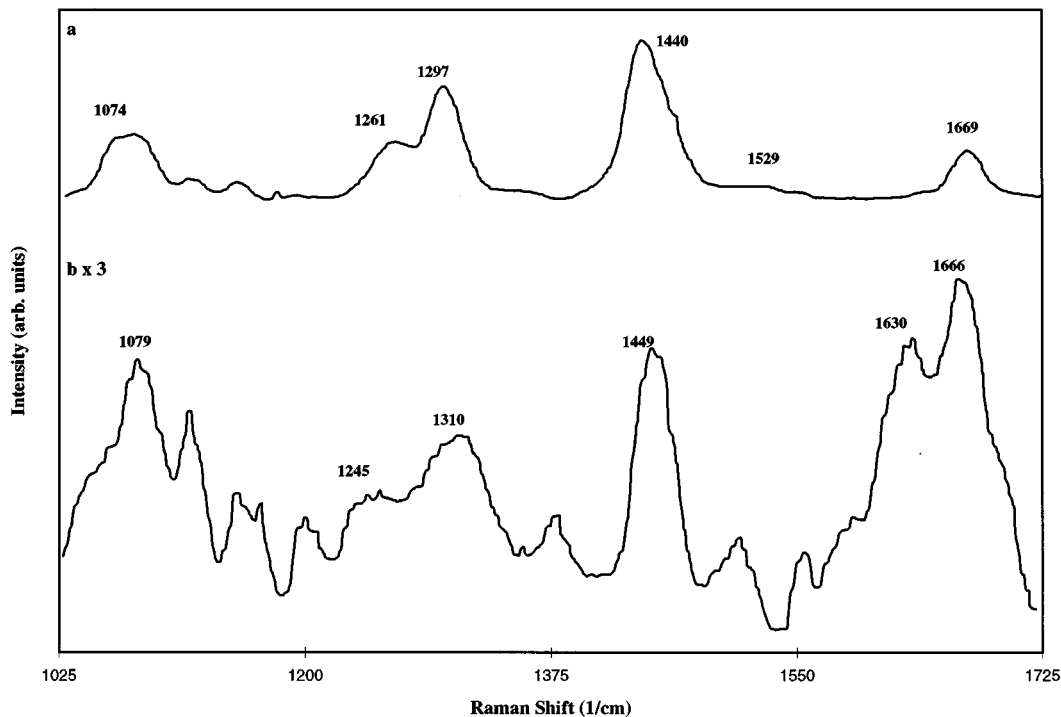
Fig. 31 NIR Raman spectra of normal human adipose tissue and lipsarcoma at 830 nm excitation (250 mW, 15 to 60 s). (Modified from Ref. 51.)

tional spectra of benign breast tissues (which include normal tissues) showed four characteristic bands at 1078, 1300, 1445, and 1651 cm^{-1}. The spectra of benign tumors showed bands at 1240, 1445, and 1659 cm^{-1} and malignant tumors displayed two Raman bands at 1445 and 1651 cm^{-1}. The intensity ratio of 1445 to 1651 cm^{-1} was found to be larger in benign tissues than in benign tumors and the same ratio was found to be even lower in malignant tumors. The diagnostic bands at 1445 (CH$_2$—CH$_3$ bend) and 1651 cm^{-1} (amide I) were assigned to proteins by Alfano et al.[70]

Raman spectroscopy using visible excitation was also used to study excised human breast tissues, and spectra characteristic of normal, fibrotic benign and malignant tissues were obtained.[60,71] Spectra were also obtained from pure compounds, and the features observed in tissue spectra were determined to be primarily due to carotenoids, myoglobin, and lipids (Fig. 32). The Raman spectra of normal breast tissues showed peaks that were assigned to carotenoids at 1005, 1157, and 1523 cm^{-1} (which were not observed with IR excitation); peaks that were assigned to lipids, primarily oleic acid derivatives at 1302, 1442, and 1653 cm^{-1}; a peak at 1370 cm^{-1} due to myoglobin; and several other smaller unassigned peaks [Fig. 32(a)]. Frank et al. proposed a different assignment of the bands at 1445 and 1653 cm^{-1} than Alfano et al. and experimentally verified their postulate that these peaks were not due to

proteins but lipids by measuring the spectra of pure lipids.[71] Although the carotenoid and lipid peaks were also present in the spectra of breast carcinomas, the carotenoid peaks were reduced in intensity and the lipid peaks were small or entirely absent [Fig. 32(b)]. The weak band at 1370 cm^{-1} that was observed in normal tissue was found to be much more significant in carcinoma samples and shifted to 1358 cm^{-1}. The lipid and carotenoid bands are present but show an overall reduction of intensity in benign breast tissues [Fig. 32(c)].

In a subsequent study by Frank, McCreery, and Redd, the feasibility of using NIR Raman spectroscopy for breast cancer detection was assessed.[10] Chromophore contributions were found to differ as excitation was shifted from the visible (which yielded carotenoid and lipid bands) to the NIR (which yielded only lipids bands) in normal tissues (Table 9). NIR Raman spectroscopy yielded signals with lower fluorescence interference and a higher S/N ratio. NIR Raman spectra were obtained from excised normal human breast tissues, tissues with fibrocystic change, and infiltrating ductal carcinoma by Frank, McCreery, and Redd.[10] NIR Raman spectra were measured at 784 nm excitation and detected using an imaging spectrograph and CCD camera. Figure 33 shows Raman spectra from normal, malignant (IDC) and benign (fibrocystic change) breast tissues. The ratio of the areas under the peaks at 1654 cm^{-1} and 1439 cm^{-1} were com-
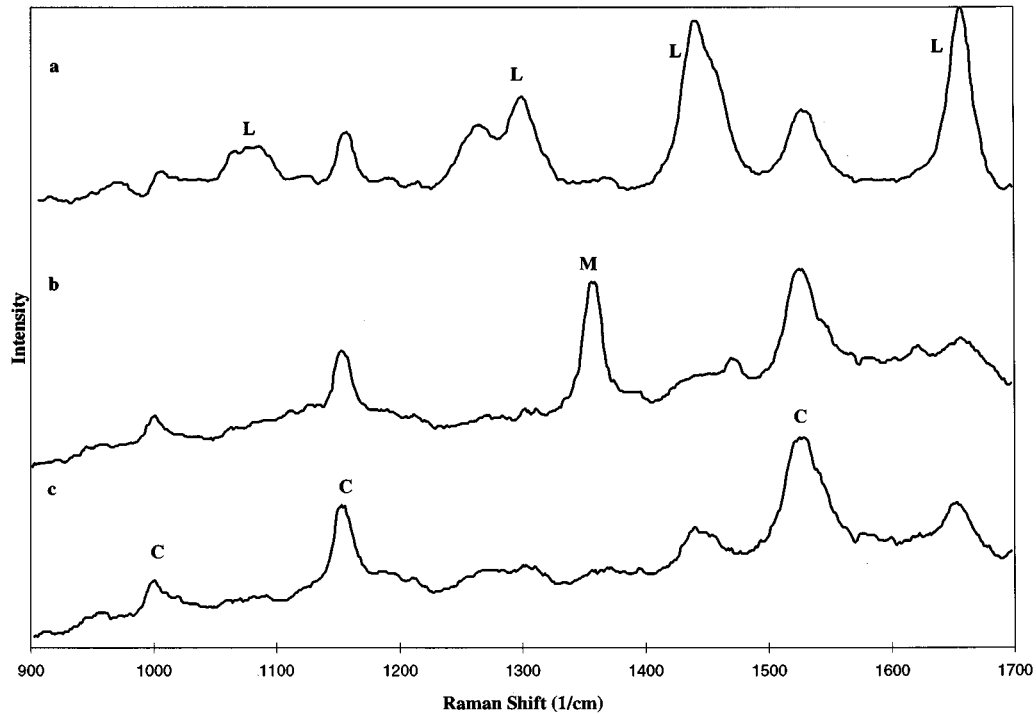
Fig. 32 Raman spectra of human breast tissue at 406.7 nm excitation: (a) normal breast tissue (50 mW, 1 to 4 s), (b) breast carcinoma (40 mW, 2.5 s), and (c) breast fibrosis (150 mW, 1 s). C-carotenoid; L-lipid, and M-myoglobin. (Modified from Ref. 60.)

Table 9 Comparison of vibrational bands observed in breast tissues at different excitation wavelengths. (Modified from Ref. 71.)

$\lambda_{exc}=$ 406 nm	$\lambda_{exc}=$ 488 nm	$\lambda_{exc}=$ 515 nm	$\lambda_{exc}=$ 647 nm	$\lambda_{exc}=$ 691 nm	$\lambda_{exc}=$ 784 nm	λ_{exc} 830 nm	Molecular Assignment
					727	727	lipid
	872				870	868	lipid
				972	972	972	lipid
1005	1006	1005					carotenoid
				1065	1066	1065	lipid
			1081	1077	1079	1079	lipid
					1119	1119	lipid
1155	1157	1156					carotenoid
	1190	1197					carotenoid
1263			1269	1265	1265	1265	lipid
1300		1305	1301	1303	1303	1303	lipid
1442	1443	1438	1439	1440	1439	1439	lipid
1526	1525	1517					carotenoid
1654	1653	1654	1654	1655	1654	1654	lipid
				1745	1743	1745	lipid

pared for normal and malignant breast tissues. The ratio for normal tissues from patients with different abnormalities varied by 5%. The area ratio increases from 0.3 in normal tissues to 1.0 in IDC samples. This increase is consistent with the changes reported by Alfano et al.[71] The intensity of the 1654 cm^{-1} C=C stretching band varies with the degree of fatty acid unsaturation and the CH$_2$ scissoring band at 1439 cm^{-1} depends on the lipid-to-protein ratio.

The spectra from IDC tissue showed an overall decrease in intensity with respect to normal tissue [Fig. 33(b)]. The peak at 1439 cm^{-1} was shifted to 1450 cm^{-1} and is attributed to the different CH$_2$ deformation frequencies in lipids and proteins. Several differences were also observed when IDC tissues were compared with benign abnormal tissue. In benign tissue, the intensities of the bands at 1656 cm^{-1} and 1259 cm^{-1} were smaller than the band at 1449 cm^{-1}, and this band is further shifted to 1446 cm^{-1} [Fig. 33(c)]. The region of 850 to 950 cm^{-1} showed only two bands in benign tissue compared with four in IDC samples. The peaks observed in normal tissues were primarily attributed to oleic acid methyl ester, a lipid, and the peaks observed in IDC and benign tissues were primarily attributed to collagen I (Table 10). This is consistent with the histopathology where IDC and benign tissues are firm and rubbery macroscopically and show an increase in interstitial tissues microscopically. Although samples from only 12 patients were studied, the spectral differences were found to be significant and warrant further pursuit. Similar results were also obtained by Feld et al. where a comparable system was used.[9]

6.3 COLON AND BLADDER CANCER

Colorectal carcinomas are generally adenocarcinomas that usually begin as polyps and evolve into other patterns. They typically secrete mucin, and invasion leads to strong stromal involvement, forming hard, firm carcinomas.[13] Preliminary work was conducted by Feld et al. using NIR Raman spectroscopy to identify colon cancer; small differences were found in the Raman spectra of normal samples and adenocarcinoma.[9] The difference spectrum formed by subtracting the spectrum of normal from carcinoma tissues shows the variations in the vibrational bands with cancer (Fig. 34). Peaks at 1662, 1576, 1458, and 1340 cm^{-1} corresponding to nucleic acid modes (purines—1576, 1458 cm^{-1}) were found to be more intense in carcinoma samples, indicating an increased nuclear content with carcinoma. In addition, several peaks corresponding to lipids were found to be more intense in normal samples.

Bladder cancers are most commonly of epithelial origin. NIR Raman spectroscopy was also used to study bladder cancers.[9] The Raman spectra were dominated by contributions from protein bands;

however, spectral differences similar to those observed in the colon were also displayed. Increased intensity of the nuclear bands was accompanied by decreased lipid bands in bladder cancer samples relative to normal samples.

6.4 CANCER OF GYNECOLOGIC TISSUES

Liu et al. were the first to report on the feasibility of using FT-IR Raman spectroscopy for detecting cancers originating from various gynecologic tissues.[8] Characteristic features of normal tissues and malignant tumors from the cervix, uterus, endometrium, and ovary were described. The gynecologic tissues studied differ structurally as well as functionally.[13,68] The ectocervix consists of nonkeratinizing squamous epithelium with an underlying collagenous stroma. Cervical cancers are primarily epithelial in origin and can be detected in their precancerous stage with routine cytologic screening. The ecto- and endocervix are separated by the squamocolumnar junction with the endocervix tran-
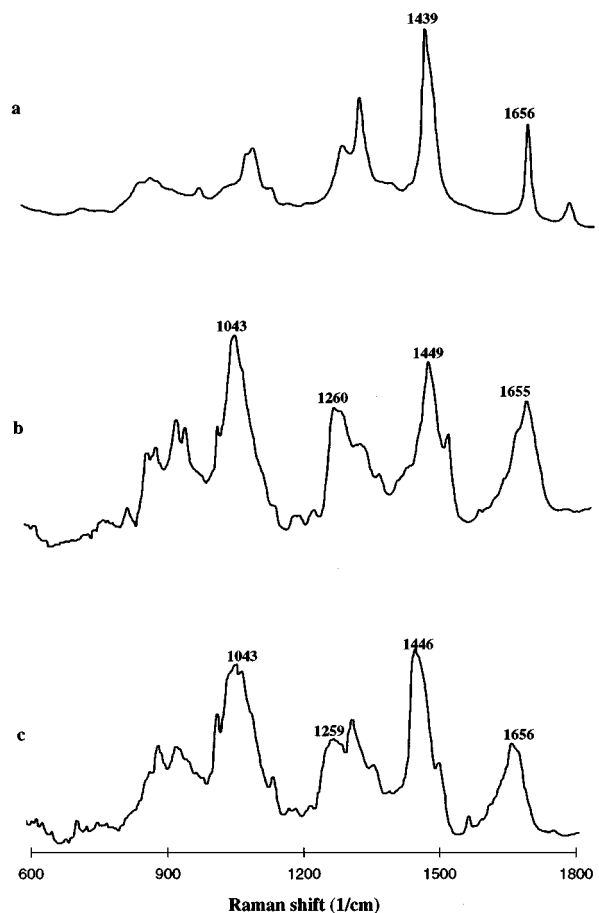

Fig. 33 Raman spectra of human breast tissue at 784 nm excitation: (a) normal breast tissue (100 mW, 300 s), (b) infiltrating ductal carcinoma (100 mW, 300 s), and (c) tissue with fibrocystic change (200 mW). Sloping baseline was subtracted from all spectra. (Modified from Ref. 10.)

Table 10 Summary of vibrational bands observed in normal and malignant breast tissues and the corresponding biological constituents. (Adapted from results in Ref. 10.)

Normal	Oleic Acid Methyl Ester	Bond Assignment	IDC	Collagen Type I	Bond Assignment
727	728	=C—H in plane bend	817	814	C—C stretch
849	856		856	855	C—C stretch
870	868		876	874	C—C stretch
890	887		920	920	C—C stretch
972	973	=C—H off plane deform	937	934	C—C stretch
1005[1]		carotenoid	1004[3]	1002	phenylalanine
1066	1067	C—C stretch	1043	1032	proline
1079	1082	C—C stretch	1125	1127	
1119	1118	C—C stretch	1157[1]		carotenoid
1157[1]		carotenoid	1167	1166	
1190[1]		carotenoid	1190[1]		carotenoid
			1206	1206	hydroxyproline, tyrosine
			1247	1247	amide III
1265	1268	=C—H in plane deform	1267	1269	amide III
1303	1304	CH_2 twist	1303	1319	CH_3, CH_2 twist
			1343	1343	CH_3, CH_2 wag
1370[2]		myoglobin	1358[2]		myoglobin
1439	1442	CH_2 scissors	1450	1451	CH_3, CH_2 deform
1523[1]		carotenoid	1525[1]		carotenoid
			1554	1554	
1654	1655	C=C stretch	1657	1665	amide I
1743	1743	C=O stretch			

[1] These are carotenoid bands seen only with visible excitation.

[2] This band is assigned to myoglobin and seen only with visible excitation.

[3] This band is assigned to collagen at NIR excitation and carotenoids at visible excitation.

scending into a mucus-secreting columnar epithelium. Endocervical cancers are typically adenocarcinomas and arise within the endocervix, as opposed to cervical epithelial lesions, which arise in the squamocolumnar junction. The uterus is a thick muscular organ; the muscle is the myometrium and its mucus lining membrane is the endometrium. The endometrium changes with menstruation and its corresponding hormonal cycle; it varies from proliferative growth of stroma and glands to becoming soft and fatty to shedding two-thirds of its structure. Uterine and endometrial cancers may arise from the glands, stroma, or smooth muscles. Most endometrial cancers are adenocarcinomas characterized by well-defined glandular patterns

lined with columnar epithelial cells. Ovaries are made up of bilayered cortex, with a layer of fibroblasts and a layer of collagenous connective tissue and medulla consisting of mesenchymal tissue and steroid-producing cells. Most ovarian cancers arise from the surface epithelium. The tumors may be cystic, fibrous, or a mixture of the two. They are generally nonfunctional and hence hard to detect until their final stages.

Three significant peaks were noted to differ in the Raman spectra of normal and benign cervix compared with cancerous lesions. In cancerous tissues, the intensity of the amide I stretching vibration band at 1657 cm^{-1} is less than the intensity of the
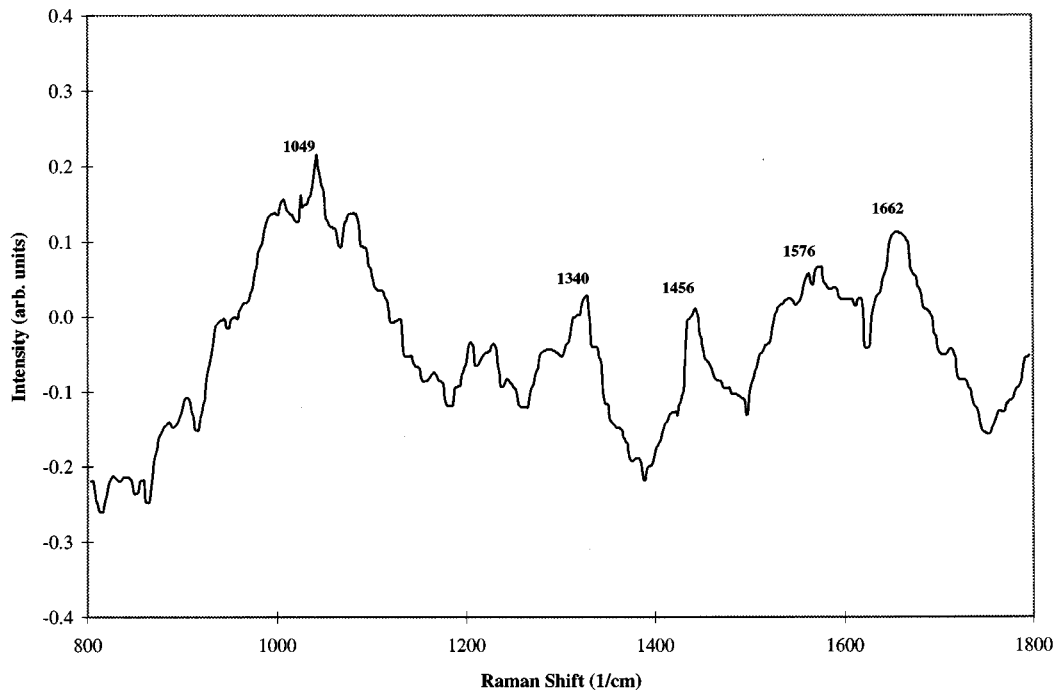
Fig. 34 Difference spectra of human adenocarcinoma and normal colon samples from the same patient at 830 nm excitation (60 to 480 mW, 1 min). (Modified from Ref. 9.)

C—H bending vibrational band at 1445 cm^{-1}. The amide III band at 1262 cm^{-1} is broadened in cancerous lesions. An additional unidentified peak at 934 cm^{-1} is observed only in normal and benign cervical samples. A possible diagnostic algorithm could be based on the relative intensities of the two peaks where $I_{1657} > I_{1445}$ in normal and benign tissues and $I_{1657} < I_{1445}$ in cancerous samples. These peaks were primarily attributed to collagen and elastin by Alfano et al.[8]

The intensity ratio of 1657 cm^{-1} to 1445 cm^{-1} could be used to differentiation in other gynecologic tissues as well. The peaks at 1262, 1445, and 1657 cm^{-1} were consistently observed (see, for example, Fig. 35). In uterine samples, the behavior of the intensity ratio was similar to that in the cervix. I_{1657}/I_{1445} was greater than one in normal and cancerous endometrial samples. In ovarian tissues, $I_{1657} < I_{1445}$ in normal ovary and $I_{1657} > I_{1445}$ in malignant samples. The bands were shifted to 1651 and 1453 cm^{-1} in malignant ovarian tissues. These peaks were primarily assigned to collagen and/or elastin in the different tissues (Table 11). However, in fatty tissues such as the endometrium, the previously assigned amide bands at 1262 and 1656 cm^{-1} were attributed to lipids instead.

Although Raman spectra were obtained from normal, "benign," and malignant cervical tissues, Alfano et al. did not attempt to differentiate between normal tissues and precancerous lesions. The potential of NIR Raman spectroscopy to differentiate cervical precancers from normal tissues, inflammation, and metaplasia and to differentially diagnose low-grade and high-grade precancers has been studied by our group.[11,25] Cervical precancers are confined to the epithelium; they arise from the basal layers and progress to the top. Inflammation and metaplasia are benign processes that are usually of little clinical consequence. These processes cause activity in the epithelium as well as the stroma;[72] thus the increased penetration of NIR excitation may allow recognition of inflammation and metaplasia.

NIR Raman spectra were measured using 789-nm excitation from normal, benign (inflammation and metaplasia), and precancerous biopsies.[11] Raman spectra from normal and precancerous tissues, indicating several spectral features with diagnostic potential, are shown in Figure 36. The intensity of the amide I band at 1656 cm^{-1} was lower in precancerous tissues than in other tissue categories. The band at 1325 cm^{-1} was attributed to nucleic acids and was found to be more intense in precancerous tissues. A diagnostic algorithm based on the intensity at 1656 cm^{-1} could differentiate precancers from other tissue categories with a false negative rate of 9% and a flash positive rate of 12% in a paired analysis, which was obtained by normalizing the peak of an unknown sample to that of a known normal from the same patient.

The amide I band can further separate previously classified precancers at high-grade and low-grade precancers with a false negative rate of 14% and a false positive rate of 4%. In addition, the ratio of
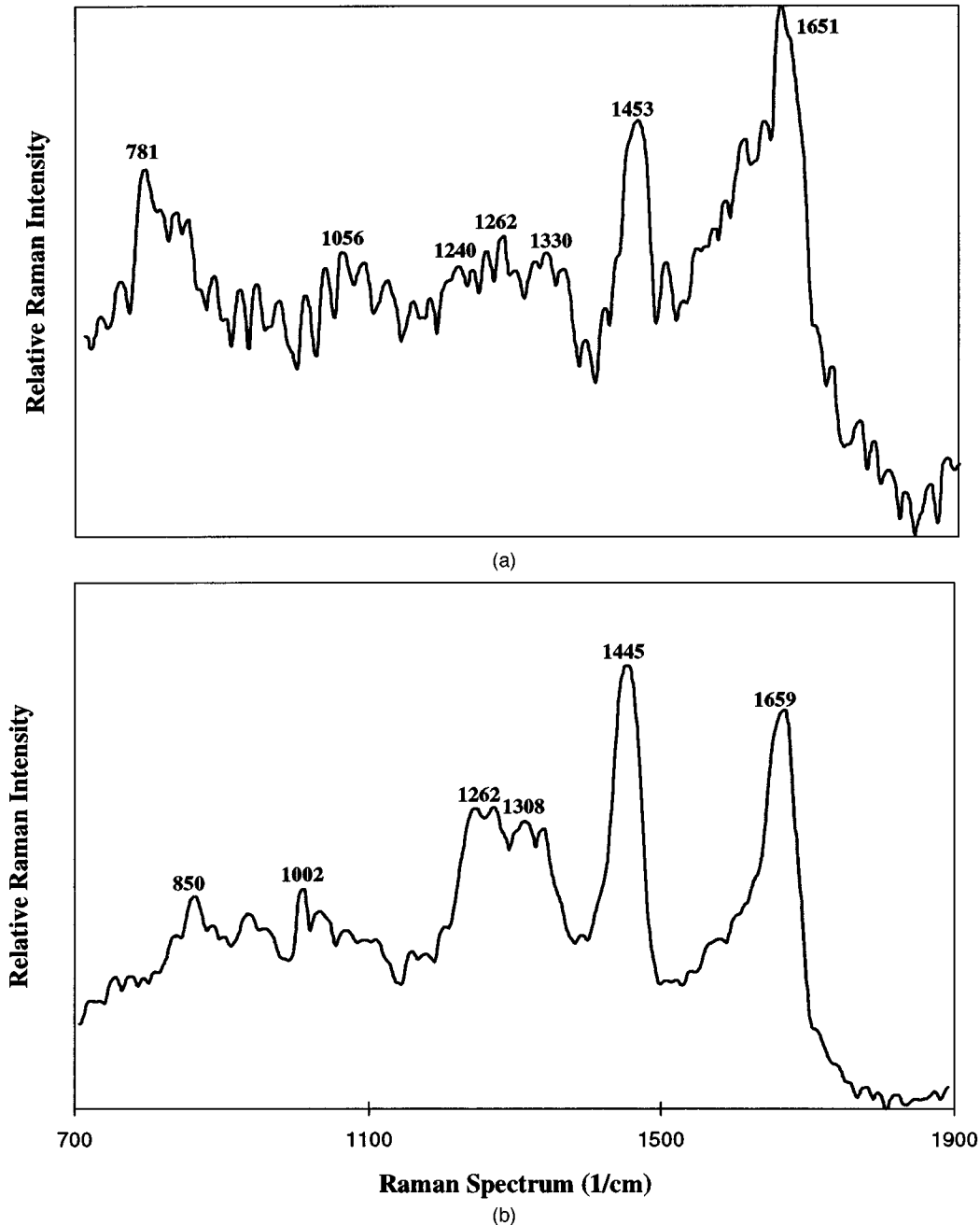
Fig. 35 FT Raman spectra of human ovarian tissue at 1064 nm excitation (1 W, 800 scans): (a) malignant ovarian tissue and (b) normal ovarian tissue. (Modified from Ref. 8.)

unnormalized intensities at 1656 to 1325 cm^{-1} (amide proteins to nucleic acid bands) could separate precancers from all other tissue categories with a false negative and false positive rate of 18% and 20%, and the ratio of unnormalized intensities at 1656 to 1454 cm^{-1} (amide proteins to protein or lipid bands) was used to separate high-grade and low-grade precancers with a false negative and false positive rate of 0% without the need for spectra from a known normal sample. Multivariate sta-

tistical techniques were also used for analysis and classification to include all the available spectral information. Intensities at eight frequencies were identified and used to differentiate precancers from all other tissue categories under cross validation with a false negative and false positive rate of 18% and 4% (Fig. 37). These results suggest the potential of near-infrared Raman spectroscopy for diagnosing cervical precancer. Inflammation and metaplasia samples can be separated from precancerous

Table 11 Summary of vibrational bands and their assignment observed in gynecologic tissues. (Adapted from results in Ref. 8.)

Cervix		Uterus		Endo		Ovary		Bond Assignment	Molecular Assignment
Benign	Malign	Benign	Malign	Benign	Malign	Benign	Malign		
							781		
	827			819	819			C—H off plane bend	blood, tyrosine
850		850	850			850		proline	collagen, elastin
934		934	934						
1002	1002	1002	1002	1002	1002	1002		C—H off plane bend	blood
							1056		lipid
			1240				1240		elastin
1262	1270	1262	1262	1262	1262	1262	1262	amide III	collagen, elastin
	1300		1315	1300	1300	1308		C—H bend	lipid
	1330		1330				1330		tryptophan
1445	1445	1453	1445	1445	1450	1445	1453	CH_2—CH_3 bend	lipid
1659	1657	1659	1659	1656	1655	1659	1651	amide I	collagen, elastin
$I_{1659}>$	$I_{1659}<$	$I_{1659}>$	$I_{1659}<$	$I_{1656}>$	$I_{1655}>$	$I_{1659}<$	$I_{1659}>$		
I_{1445}	I_{1445}	I_{1453}	I_{1445}	I_{1445}	I_{1450}	I_{1445}	I_{1443}		

samples using any of the algorithms described above, obviating a potential limitation of fluorescence spectroscopy-based algorithms.

6.5 SUMMARY OF RESULTS

Tables 9 to 11 effectively summarize some of the results obtained from the application of Raman spectroscopy to cancer detection. The abundance of diagnostic features in the tissue spectra clearly indicate the potential of this technique for clinical application. In comparing the fingerprint features of the Raman spectra from different tissues and their cancers, several similarities and differences were observed. The ratio of intensities at 1655 cm^{-1} to 1450 cm^{-1} has been consistently used to differentiate normal and cancerous tissues at different sites, including brain, breast, and gynecologic tissues. In several tissues, the second amide band at 1260 cm^{-1} contributes toward differentiation as well. In addition, cancers show a significant nucleic acid contribution compared with normal tissues and can be used as a diagnostic tool.[9,11] On the other hand, fatty tissues such as breast and endometrium show identical peaks assigned to lipids.[8]

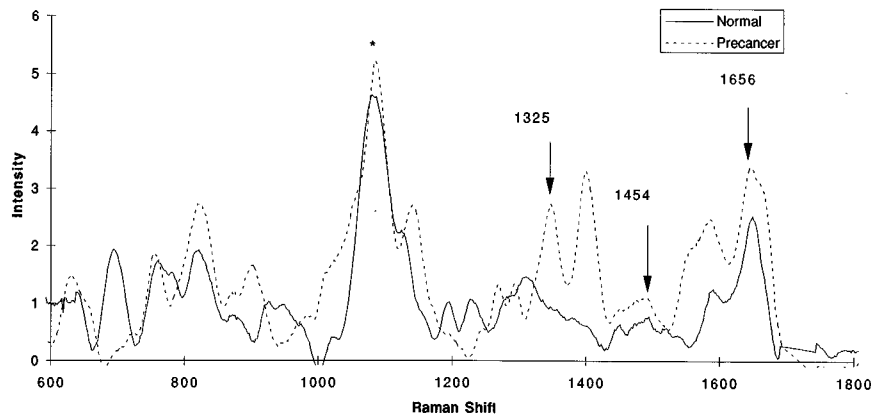The Raman spectra of normal, precancerous, and cancerous tissues contain contributions from bio-

Fig. 36 Raman spectra of normal and precancerous human cervical tisse at 789 nm excitation (25 mW, 15 min). (Modified from Ref. 11.)
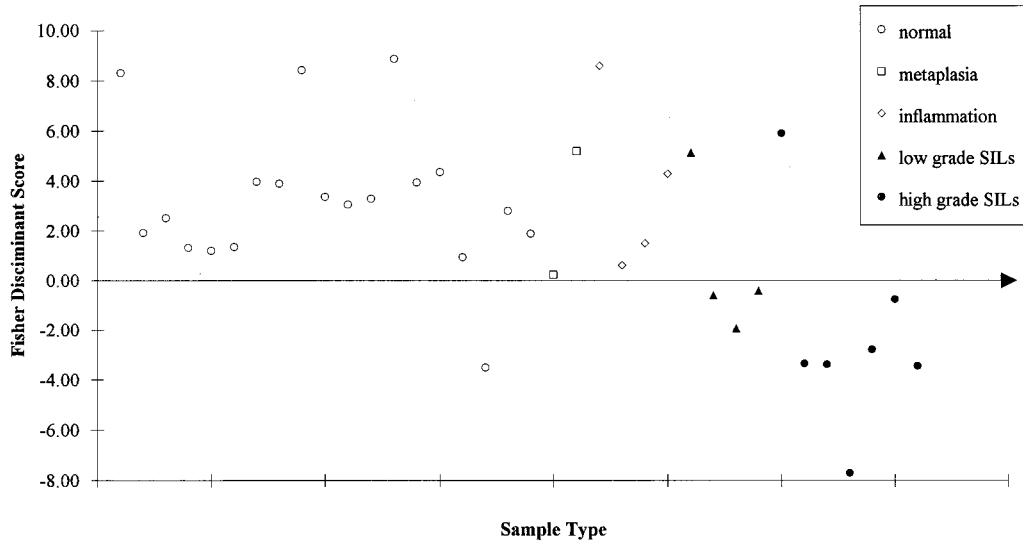
Fig. 37 Multivariate diagnostic algorithm based on PCA and FDA for differentiating human cervical precancers from all other cervical tissues using intensities at eight frequencies. The decision line separates precancers from all other cervical tissues with a sensitivity and specificity of 82 and 96%. (Modified from Ref. 11.)

logical molecules that depend on the microscopic environment in tissues and interactions with each other. Tissue Raman spectra show primary contributions from proteins, lipids, and nucleic acids. However, identification of specific molecular conformations in gross tissue is made difficult by the very changes that characterize them in their environment. The potential to derive more detailed biochemical information is present, but realizing it will require detailed microscopic and chemical studies using techniques described in the molecular and cellular sections of this paper.

7 CLINICAL APPLICATION OF RAMAN SPECTROSCOPY

In order to fully evaluate the potential of Raman spectroscopy for clinical detection of precancers and cancers, *in vivo* studies are required. Several groups have initiated this process with varying degrees of success. This progression has been made possible by the development of sensitive instrumentation, use of fiber optics, and development of automated algorithms.

7.1 AUTOMATED DIAGNOSIS

One of the potential advantages of spectroscopic diagnosis is automation, which allows objective and real-time diagnosis of pathologies. Differences in spectral features can be incorporated in diagnostic algorithms; several techniques have been identified and used to enhance the differentiation and classification of tissues for potential automated, clinical diagnosis. The simplest algorithms are based on empirically identified diagnostic features. These differences may be variations in intensity, intensity

ratios, and number and location of peaks. For example, the intensity ratio of the CH_2 bending vibrational mode at 1450 cm^{-1} to the amide I vibrational mode at 1655 cm^{-1} has been observed to vary with disease in several applications, including breast cancers and gynecologic cancers and precancers.[8,11,73] Often, several spectral features contribute to the differences observed in normal and abnormal tissues, and more elaborate techniques such as multivariate statistical methods may improve differentiation. Partial least squares, a regression-based technique, was used to extract accurate concentrations of dissolved glucose and bicarbonate using NIR Raman spectra for transcutaneous blood analysis.[74] Mahadevan-Jansen et al. developed a multivariate algorithm in which principal component analysis (PCA) was used for data reduction and Fischer discriminant analysis (FDA) was used for the classification.[11] Lewis et al. used neural networks and a learning algorithm to classify wood with Raman spectroscopy.[75] Several other techniques have also been attempted. These include building a library of known spectra that was used to classify the origin of tissue based on its Raman spectra.[61] These and other techniques allow automated diagnosis that enhances the potential of real-time clinical detection of disease.

7.2 FIBER OPTIC REMOTE SENSING

With the development and availability of diode lasers, imaging spectrographs, and cooled CCD cameras, it became possible to build compact NIR Raman systems that acquire spectra with short integration times.[9,10] Fiber optic probes can be designed to deliver and collect signal efficiently, thus allowing remote access. However, a significant

problem with this idea has been that of signals generated by the fibers themselves (luminescence and Raman).[76] The signal generated is proportional to the fiber length and limits the detection capability of the technique.[77] Figure 38 shows the Raman spectra of fused silica (Diaguide fiber from Mitsubishi Cable) used to design a probe. A Raman signal was observed to be generated from the core [Fig. 38(a)] as well as the cladding and buffer [Fig. 38(b)] of the fiber.[76] This signal can have magnitudes equal to and sometimes greater than that of the sample under study and thus needs careful consideration.[77] Fiber signal is generated in the delivery fiber by the excitation light. In addition, background signal is also generated in the collection fibers by the elastically scattered excitation light returning into the collection fiber(s). A feasible probe design must prevent unwanted signal generated in the delivery fiber from illuminating the sample as well as preventing elastically scattered excitation light from entering the collection fibers and generating unwanted signal.

Several different designs have been proposed for potential clinical acquisition of Raman spectra using fiber optic probes. Myrick and Angel developed different dual fiber probes which could be used under different conditions with maximum collection efficiency but minimum fiber interference (Fig. 39).[77] One of these probes, which can potentially be used *in vivo*, consists of separate single fibers for delivery and collection placed at a small angle relative to each other. Graded index lenses and Winston cones were used at the distal tip of the fibers for focusing and collimating the beam. In addition, a bandpass filter was placed after the excitation fiber lens and a longpass filter was placed between the sample and collection fiber lens. Thus the bandpass filter allows only the transmission of the excitation light from the delivery fiber, and the longpass filter
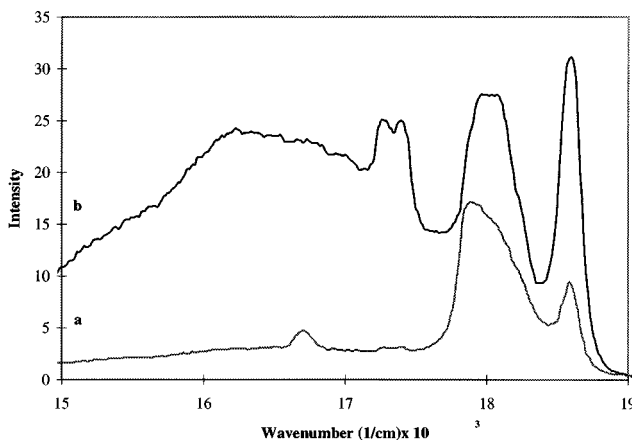
blocks the transmission of the Fresnel reflected excitation light as well as the elastically scattered light, keeping it from entering the collection fibers.

Multiple fiber bundles have been utilized for spectroscopic measurements of tissue by several groups.[21,23] Such a bundle commonly consists of a central excitation fiber surrounded by many collection fibers linearly aligned in front of the spectrometer. Schwab and McCreery have used this design and tested it on different samples.[78] Although spectra with good S/N ratios could be obtained from transparent samples, the fiber background was still a serious problem in samples with high elastic scattering such as tissue. In a subsequent breast tissue study, the same group used two different fiber optic bundles; a 6×1 fiber bundle accessible through a biopsy needle and an integrated 2×2-inch noncontact probe (DLT, Laramie, WY), and tested it on breast tissue *in vitro*.[10] Bandpass and longpass filters were used in the noncontact probe to account for fiber background. Breast Raman spectra were obtained using both probes but required long integration times for a good S/N ratio (Fig. 40).[10] Fiber interference was found to be more significant for cancer samples with both probes.

Berger et al. have developed a novel design for improved signal collection to allow spectral acquisition in a few seconds.[74] A hollow compound parabolic concentrator (CPC) was used at the distal tip of the probe to obtain seven times more signals than could be obtained using a fiber probe without the CPC. Fiber background was reduced by using a dichroic mirror and separate excitation and collection fiber geometries. Excitation light was reflected by the mirror (placed at 45 degrees to the sample normal) through the CPC onto the sample. Raman spectra were collected by the CPC and transmitted through the mirror into a collection fiber bundle (with about 100 fibers) to a detector. The dichroic mirror transmits the fiber signal from the delivery fiber and reflects the excitation and elastically scattered light, thus preventing their entry into the collection fibers; this reduces the interference of the

Fig. 38 Raman and luminescence spectra at 488 nm excitation of (a) core in a 200 μm core optical fiber from Diaguide and (b) cladding and buffer of the same optical fiber. (Modified from Ref. 76.)
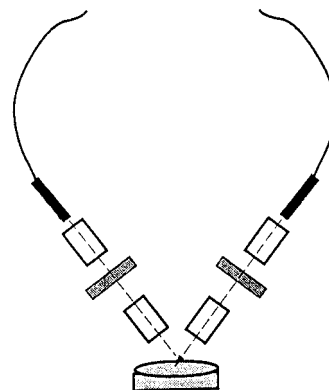

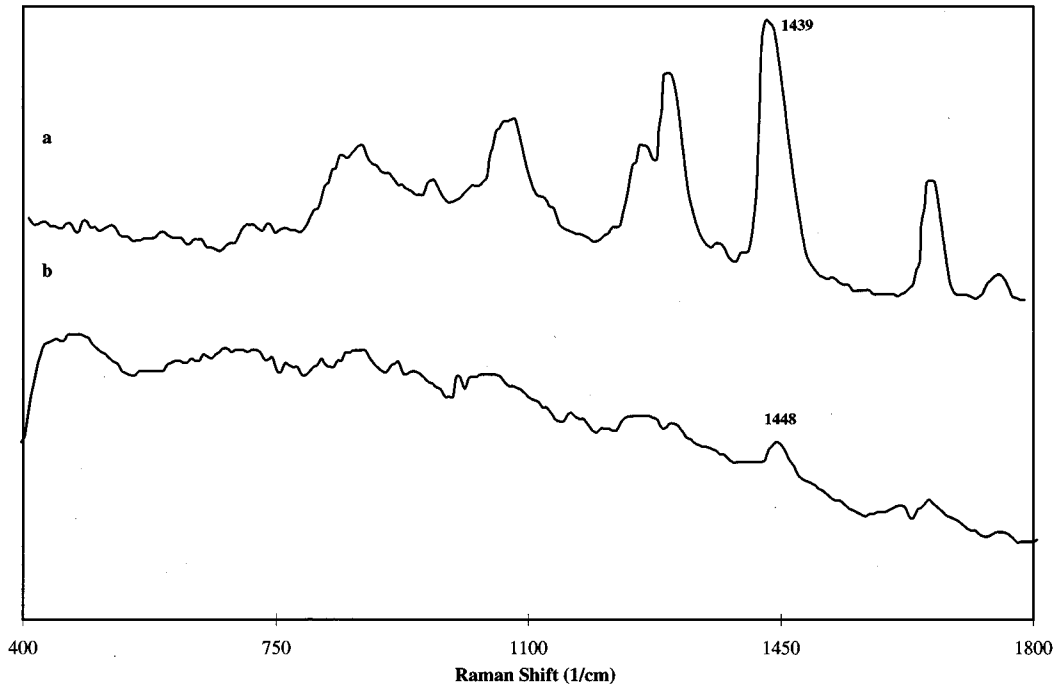**Fig. 39** Dual fiber configuration. (Modified from Ref. 77.)

Fig. 40 Raman spectra of human breast tissue at 784 nm excitation obtained with the noncontact DLT probe: (a) normal breast tissue (50 mW, 300 s) and (b) diseased breast tissue (average of 25 3-min scans). (Modified from Ref. 10.)

fiber signal from sample Raman acquisition. This probe design was used to acquire Raman spectra for transcutaneous blood glucose measurements.

Other successful *in vivo* measurements have been in the eye,[79] nail,[6] and skin.[66] *In vivo* applications thus far have been confined to exposed tissue areas where fiber background could be circumvented using a macroscopic arrangement; e.g., a DLT probe for breast tissues by Frank, McCreery, and Redd[10] and a CPC probe for transcutaneous measurements of blood analytes by Bergen, Itzkan, and Feld.[74] However, other applications such as in the colon, cervix, and oral cavity, require a more compact configuration and probe design. Although several groups have concentrated their efforts in this direction, we were unable to find any reports of success thus far.

7.3 TEMPERATURE CONSIDERATIONS

Application of any technique that uses lasers must follow certain safety standards to avoid potential hazards. Safety standards for laser exposure of skin and eye have been set by the American National Standards Institute (ANSI). The power densities used for successful Raman spectral acquisitions can be quite high and warrant consideration of safety hazards. The maximum permissible exposures as set by ANSI are wavelength dependent and can be calculated for a given exposure time following the directions laid out in the ANSI laser safety manual.[80] For example, for continuous wave light at 790 nm excitation, the ANSI safety standard is 0.3

W/cm^2 (for greater than 10 s exposure) for the skin. This corresponds to 99 μW of power for a 200 μm spot size, which we find insufficient to generate detectable Raman signal from the human cervix. Thus we have explored supplementary methods of analysis to investigate the potential thermal effects of laser exposures in excess of those set by the ANSI standards for skin.

Simulations were performed to calculate the expected rise in temperature due to laser radiation exceeding the ANSI threshold in Raman measurements of tissues. Light distribution was simulated using a Monte Carlo model for specific conditions and using optical properties from the literature. This was followed by thermal calculations using an implicit finite difference thermal model.[81] The thermal model assumes no perfusion and an air medium surrounding the tissue during irradiation. The model does not take into consideration the cooling effects of evaporation; this can result in an overestimation of the rise in temperature by this model.[82] For cervical tissue, a 25 mW source with a spot size of 500 μm at 789 nm corresponds to 40 times the power density safely allowed by ANSI for skin. The simulation calculated a rise in temperature of only 5.6 °C/min for the same parameters. On the other hand, many groups typically use higher powers for Raman signal collection. In an *in vitro* study by Kramer et al., Raman spectra were collected from coronary arteries using 830 nm excitation, 350 mW power, incident in a 1-mm spot.[83] This corresponds to 122 times the minimal permis-

sible exposure set by ANSI for skin, and the model yields a temperature rise of 60 °C/min. Although the model may overestimate the rise in temperature, the results clearly indicate that the use of high power must be accompanied by temperature calculations to ascertain that spectra are not being measured from thermally damaged tissue.

8 PERSPECTIVES ON THE FUTURE

This paper reviews the use of nonresonance Raman spectroscopy to detect precancers and cancers. The success of the technique has led to the development of feasible clinical systems that can measure Raman signals from tissue with short collection times.[9,10] For example, Frank, McCreery, and Redd describe the use of two potentially clinical fiber optic probes: one for noncontact measurements and one accessible through the biopsy channel.[10] Although measurements were not performed *in vivo*, the probes were tested on a model of breast tissues. Kramer et al. have developed a clinical Raman system using a uniquely designed probe incorporating a CPC, and spectra were measured from coronary arteries *in vitro*.[83] *In vivo* studies were stated to be in progress. These studies clearly indicate that successful clinical application of Raman spectroscopy is imminent and may be expected to change the face of cancer detection in the near future.

The complexity of tissue structure and environment make the interpretation of tissue Raman spectra difficult. To achieve the maximum benefit from Raman-based diagnostic systems, an understanding of the molecular, microscopic, and macroscopic origin of observed tissue Raman signals is required. *In vitro* results have demonstrated contributions from proteins, lipids, and nucleic acids which are altered under neoplastic transformations. However, despite the ability of Raman spectroscopy to probe molecular conformations and interactions of samples in solution and in single cells, this degree of information has not yet been obtained from tissue Raman spectra. Extracting this information will require more detailed chemical and microscopic studies to confirm the molecular basis of tissue signals and the development of models to relate the macroscopic signal to its microscopic origins. This process has been initiated with the analysis of Raman spectra from arterial tissue by Baraga, Feld, and Rava to obtain relative contributions from participating chromophores.[84] We believe that using similar tools to analyze the Raman spectra of neoplastic tissues will yield results that will maximize the clinical potential of this technique.

Acknowledgments

REFERENCES

1. P. R. Carey, *Biochemical Applications of Raman and Resonance Raman Spectroscopies*, Academic Press, New York (1982).
2. F. S. Parker, *Applications of Infrared, Raman and Resonance Raman Spectroscopy in Biochemistry*, Plenum Press, New York (1983).
3. J. Twardowski and P. Anzenbacher, *Raman and IR Spectroscopy in Biology and Biochemistry*, Ellis Horwood, New York (1994).
4. Y. Ozaki, "Medical application of Raman spectroscopy," *Appl. Spectroscopy Rev.* **24**(3&4), 259–312 (1988).
5. S. Nie, K. J. Bergbauer, J. J. Ho, J. F. R. Kuck, Jr. and N. T. Yu, "Application of near-infrared Fourier transform Raman spectroscopy in biology and medicine," *Spectroscopy* **5**, 24–32 (1990).
6. B. Schrader, S. Keller, T. Loechte, S. Fendel, D. S. Moore, A. Simon, and J. Sawatzki, "NIR FT Raman spectroscopy in medical diagnosis," *J. Mol. Struct.* **348**, 293–296 (1995).
7. J. F. Brennan, III, T. J. Romer, Y. Wang, A. M. Tercyak, M. Fitzmaurice, R. S. Lees, R. R. Dasari, J. R. Kramer and M. S. Feld, "In situ histochemical analysis of human coronary artery by Raman spectroscopy compared with biochemical assay," in *Advances in Fluorescence Sensing Technology, Vol. II,* J. R. Lakowicz, ed., SPIE Proc. **2388**, 105–109 (1995).
8. C. H. Liu, B. B. Das, W. L. Sha Glassman, G. C. Tang, K. M. Yoo, H. R. Zhu, D. L. Akins, S. S. Lubicz, J. Cleary, R. Prudente, E. Celmer, A. Caron, and R. R. Alfano, "Raman fluorescence and time-resolved light scattering as optical diagnostic techniques to separate diseased and normal biomedical media," *J. Photochem. Photobiol. B: Biol.* **16**, 187–209 (1992).
9. M. S. Feld, R. Manoharan, J. Salenius, J. Orenstein-Carndona, T. J. Romer, J. F. Brennan, III, R. R. Dasari, and Y. Wang, "Detection and characterization of human tissue lesions with near infrared Raman spectroscopy," in: *Advances in Fluorescence Sensing Technology, Vol. II,* J. R. Lakowicz, ed. Proc. SPIE **2388**, 99–104 (1995).
10. C. J. Frank, R. L. McCreery, and D. C. Redd, "Raman spectroscopy of normal and diseased human breast tissues," *Anal. Chem.* **67**(5), 777–783 (1995).
11. A. Mahadevan Jansen, M. F. Mitchell, N. Ramanujam, A. Malpica, S. Thomsen, and R. Richards-Kortum, "Near infrared Raman spectroscopy for the detection of cervical precancers," *Appl. Spectroscopy* (submitted for publication) (1995).
12. *Cancer Facts & Figures* 1994, American Cancer Society (1994).
13. S. L. Robbins, R. S. Cotran, and V. Kumar, *Pathologic Basis of Disease,* W. B. Saunders, Philadelphia (1994).
14. G. J. Kelloff, W. F. Maline, C. W. Boone, V. E. Steele, and L. A. Doody, "Intermediate biomarkers of precancers and their application in chemoprevention," *J. Cell. Biochem.* **Supp.(16G)**, 15–21 (1992).
15. E. S. Andersson, J. Johansson, K. Svanberg, and S. Svanberg, "Flourescence imaging and point measurements of tissue: Applications to the demarcation of malignant tumors and atherosclerotic lesions from normal tissue," *Photochem. Photobiol.* **53**(6), 807–814 (1991).
16. R. R. Alfano, A. Pradhan, and C. G. Tang, "Optical spectroscopic diagnosis of cancer in normal and breast tissues," *J. Opt. Soc. Am. B* **6**, 1015–1023 (1989).
17. R. R. Alfano, G. C. Tang, A. Pradhan, W. Lam, D. S. C. Choy and A. Opher, "Fluorescence spectra from cancer and normal human breast and lung tissues," *IEEE J. Quantum Electron.* **QE-23**(10), 1806–1811 (1987).
18. J. Hung, S. Lam, J. C. LeRiche, and B. Palcic, "Autofluorescence of normal and malignant bronchial tissue," *Lasers Surg. Med.* **11**, 99–105 (1991).
19. K. Roy, I. Bottrill, D. R. Ingrams, M. M. Pankratov, E. Rebeiz, P. Woo, S. Shapshay, S. Kabani, R. Manoharan, I. Itzkan, and M. S. Feld, "Diagnostic fluorescence spectroscopy of oral mucosa," in *Lasers in Surgery: Advanced Characterization, Therapeutics and Systems IV*, Proc. SPIE **2395**, 135–142 (1995).
20. N. Ramanujam, M. F. Mitchell, A. Mahadevan, S. Thomsen, E. Silva, and R. R. Richards-Kortum, "Fluorescence spectroscopy: A diagnostic tool for cervical intraepithelial neoplasia (CIN), *Gynecol. Oncol.* **52**, 31–38 (1994).
21. R. M. Cothren, R. R. Richards-Kortum, M. V. Sivak, M. Fitz-

maurice, R. P. Rava, G. A. Boyce, G. B. Hayes, M. Doxtader, R. Blackman, T. B. Ivanc, M. S. Feld, and R. E. Petras, "Gastrointenstinal tissue diagnosis by laser induced fluorescence spectroscopy at endoscopy," *Gastrointesinal Endoscopy* **36**, 105–111 (1990).

22. K. T. Schomacker, J. K. Frisoli, C. C. Compton, T. J. Flotte, J. M. Richter, N. S. Nishioka, and T. F. Deutsch, "Ultraviolet laser-induced fluorescence of colonic tissue: Basic biology and diagnostic potential," *Lasers Surg. Med.* **12**, 63–78 (1992).

23. N. Ramanujam, M. F. Mitchell, A. Mahadevan, S. Thomsen, and R. Richards-Kortum "*In Vivo* diagnosis of cervical intraepithelial neoplasia (CIN) using 337 nm laser induced fluorescence," *Proc. Nat. Acad. Sci. U.S.A.* **91**, 10193–10197 (1994).

24. N. Ramanujam, M. F. Mitchell, A. Mahadevan, S. Thomsen, A. Malpica, T. Wright, N. Atkinson, and R. Richards-Kortum, "Spectroscopic diagnosis of cervical intraepithelial neoplasia (CIN) in vivo using laser-induced fluorescence spectra at multiple excitation wavelengths," *Lasers Surg. Med.* (in press) (1995).

25. A. Mahadevan, N. Ramanujam, M. F. Mitchell, A. Malpica, S. Thomsen, and R. Richards-Kortum, "Optical techniques for the diagnosis of cervical precancers: Comparison of Raman and fluorescence spectroscopies," in *Advances in Fluorescence Sensing Technology II,* J. R. Lakowicz, ed., Proc. SPIE **2388**, 110–120 (1995).

26. S. A. Asher, "UV resonance Raman spectroscopy for analytical, physical, and biophysical chemistry," *Anal. Chem.* **65**(2), 59A–66A; 201A-209A (1993).

27. M. S. Feld and J. R. Kramer, "Mutagenicity and the XeCl excimer laser: A relationship of consequence?" *Am. Heart J.* **122**, 1803–1805 (1991).

28. L. Stryer, *Biochemistry*, W. H. Freeman, New York (1988).

29. R. Y. Yada, R. L. Jackman, and S. Nakai, "Secondary structure prediction and determination of proteins—A review," *Int. J. Peptide Protein Res.* **31**(1), 98–108 (1988).

30. J. L. Lippert, D. Tyminski, and P. J. Desmeules, "Determination of the secondary structure of proteins by laser Raman spectroscopy," *J. Am. Chem. Soc.* **98**, 7075–7080 (1976).

31. M. Pezolet, M. Pigeon-Gosselin, and L. Coulomb, "Laser Raman investigation of the conformation of human immunoglobulin G," *Biochim. Biophys. Acta* **453**(2), 502–512 (1976).

32. R. W. Williams, "Estimation of protein secondary structure from the laser Raman amide I spectrum," *J. Mol. Biol.* **166**(4), 581–603 (1983).

33. A. J. P. Alix, M. Berjot, and J. Marx, *Spectroscopy of Biological Molecules*, Wiley, Chichester (1985).

34. R. W. Williams, "Protein secondary structure analysis using Raman amide I and amide III spectra," *Meth. Enzymol.* **130**, 311–331 (1986).

35. O. Kennard and W. N. Hunter, "Oligonucleotide structure: A decade of results from single crystal X-ray diffraction studies," *Quart. Rev. Biophys.* **22**(3), 327–379 (1989).

36. T. A. Steitz, "Structural studies of protein-nucleic acid interaction: The sources of sequence-specific binding," *Quart. Rev. Biophys.* **23**(3), 205–280 (1990).

37. W. L. Peticolas and E. Evertsz, "Conformation of DNA in vitro and in vivo from laser Raman scattering," *Meth. Enzymol.* **211**, 335–352 (1992).

38. J. Duguid, V. A. Bloomfield, J. Benevides, and G. J. Thomas, Jr., "Raman spectroscopy of DNA–metal complexes. I. Interactions and conformational effects of the divalent cations: Mg, Ca, Sr, Ba, Mn, Co, Ni, Cu, Pd, and Cd," *Biophys. J.* **65**(5), 1916–1928 (1993).

39. T. M. Przybycien, J. P. Dunn, P. Valax, and G. Georgiou, "Secondary structure characterization of beta-lactamase inclusion bodies," *Protein Engineering* **7**(1), 131–136 (1994).

40. S. Zigman, T. Paxhia, T. McDaniel, M. F. Lou, and N. T. Yu, "Effect of chronic near-ultraviolet radiation on the gray squirrel lens *in vivo*," *Invest. Opthalmol. Visual Sci.* **32**(6), 1723–1732 (1991).

41. N. V. Hud, F. P. Milanovich, and R. Balhorn, "Evidence of novel secondary structure in DNA-bound protamine is revealed by Raman spectroscopy," *Biochem.* **33**(24), 7528–7535 (1994).

42. K. L. Aubrey and G. J. J. Thomas, "Raman spectroscopy of filamentous bacteriophage Ff (fd, M13,f1) incorporating specifically-deuterated alanine and tryptophan side chains. Assignments and structural interpretation," *Biophys. J.* **60**(6), 1337–1349 (1991).

43. K. L. Aubrey, S. R. Casjens, and G. J. Thomas, Jr., "Secondary structure and interactions of the packaged dsDNA genome of bacteriophage P22 investigated by Raman difference spectroscopy," *Biochemistry* **31**(47), 11835–11842 (1992).

44. G. J. Puppels, C. Otto, J. Greve, M. Robert-Nicoud, D. J. Arndt-Jovin and T. M. Jovin, "Raman microspectroscopic study of low-pH-induced changes in DNA structure of polytene chromosomes," *Biochemistry* **33**(11), 3386–3395 (1994).

45. G. J. Puppels, J. H. Olminkhof, G. M. Segers-Nolten, C. Otto, F. F. deMul, and J. Greve, "Laser irradiation and Raman spectroscopy of single living cells and chromosomes: Sample degradation occurs with 514.5 nm but not with 660 nm laser light," *Exp. Cell Res.* **195**(2), 361–367 (1991).

46. G. J. Puppels, H. S. Garritsen, G. M. Segers-Nolten, F. F. de Mul, and J. Greve, "Raman microspectroscopic approach to the study of human granulocytes," *Biophys. J.* **60**(5), 1046–1056 (1991).

47. S. P. Verma and N. Sonwalkar, "Structural changes in plasma membranes prepared from irradiated chinese hamster V79 cells as revealed by Raman spectroscopy," *Radiat. Res.* **126**(1), 27–35 (1991).

48. N. T. Yu and E. J. East, "Laser Raman spectroscopic studies of ocular lens and its isolated protein fractions," *J. Biol. Chem.* **250**, 2196–2202 91975).

49. R. H. Clarke, E. B. Hanlon, J. M. Isner, and H. Brody, "Laser Raman spectroscopy of calcified atherosclerotic lesions in cardiovascular tissue," *Appl. Opt.* **26**(16), 3175–3177 (1987).

50. J. J. Baraga, M. S. Feld, and R. P. Rava, "Rapid near-infrared Raman spectroscopy of human tissue with a spectrograph and CCD detector," *Appl. Spectrosc.* **46**(2), 187–190 (1992).

51. R. Manoharan, Y. Wang, N. Boustany, J. F. Brennan, III, J. J. Baraga, R. R. Dasari, J. Van Darn, S. Singer, and M. S. Feld, "Raman spectroscopy for cancer detection: Instrumentation development and tissue diagnosis," in *Proceedings of the Biomedical Optoelectronic Devices and Systems, Vol. II,* Proc. SPIE **2328**, 128–132 (1994).

52. J. R. Lakowicz, *Principles of Flourescence Spectroscopy*, Plenum Press, New York (1983).

53. J. M. Friedman and R. M. Hochstrasser, "The use of fluorescence quenchers in resonance Raman spectroscopy," *Chem. Phys. Lett.* **33**, 225–227 (1975).

54. R. P. Van Duyne, D. L. Jeanmaire, and D. F. Shriver, "Mode-locked laser Raman spectroscopy-a new technique for the rejection of interfering background luminescence signals," *Anal. Chem.* **46**, 213–222 (1974).

55. P. A. Mosier-Boss, S. H. Lieberman, and R. Newberry, "Fluorescence rejection in Raman spectroscopy by shifted-spectra, edge detection, and FFT filtering techniques," *Appl. Spectrosc.* **49**(5), 630–638 (1995).

56. S. M. Angel, M. K. DeArmond, K. W. Hanck, and D. W. Wertz, "Computer-controlled instrument for the recovery of a resonance Raman spectrum in the presence of strong luminescence," *Anal. Chem.* **56**, 3000–3001 (1984).

57. J. Funfschilling and D. F. Williams, "CW laser wavelength modulation in Raman and site selection fluorescence spectroscopy," *Appl. Spectrosc.* **30**(4), 443–446 (1976).

58. A. P. Shreve, N. J. Cherepy, and R. A. Mathies, "Effective rejection of fluorescence interference in Raman spectroscopy using a shifted excitation difference technique," *Appl. Spectrosc.* **46**(4), 707–711 (1992).

59. A. C. C. Bot, "Raman microspectroscopy of fixed rabbit and human lenses and lens slices: New potentialities," *Exp. Eye Res.* **49**, 161–169 (1989).

60. D. C. B. Redd, Z. C. Feng, K. T. Yue, and T. S. Gansler, "Raman spectroscopic characterization of human breast tissues: Implications for breast cancer diagnosis," *Appl. Spectrosc.* **47**(6), 787–791 (1993).

61. S. Keller, B. Schrader, A. Hoffmann, W. Schrader, K. Metz, A. Rehlaender, J. Pahnke, M. Ruwe, and W. Budach, "Application of near-infrared-Fourier transform Raman spectroscopy in medical research," *J. Raman Spectrosc.* **25**(7–8), 663–671 (1994).

62. W. Bloom and D. W. Fawcett, *A Textbook of Histology*, W. B. Saunders, Philadelphia (1980).
63. N.-T. Yu, D. C. DeNagel, P. L. Pruett, and J. F. R. Kuck, Jr., " Disulfide bond formation in the eye lens," *Proc. Natl. Acad. Sci. U.S.A.* **82**, 7965–7968 (1985).
64. A. C. Williams, B. W. Barry, and H. G. Edwards "Comparison of Fourier transform Raman spectra of mammalian and reptilian skin," *Analyst.* **119**(4), 563–566 (1994).
65. A. C. Williams, B. W. Barry, H. G. Edwards, and D. W. Farwell, "A critical comparison of some Raman spectroscopic techniques for studies of human stratum corneum," *Pharm. Res.* **10**(11), 1642–1647 (1993).
66. A. J. Welch, R. Richards-Kortum, E. Chan, G. Criswell, C. Gardner, J. Pfefer, K. Pope, and S. Warren, "Propagation of fluorescence light," (in preparation) (1995).
67. R. Manoharan, Y. Wang, R. R. Dasari, S. S. Singer, R. P. Rava, and M. S. Feld, "Ultraviolet resonance Raman spectroscopy for detection of colon cancer," *Lasers Life Sci.* **6**(4), 217–227 (1995).
68. E. Pearce, *Anatomy and Physiology for Nurses*, Oxford Univ. Press, New York (1989).
69. A. Mizuno, H. Kitajima, K. Kawauchi, S. Muraishi, and Y. Ozaki, "Near-infrared Fourier transform Raman spectroscopic study of human brain tissues and tumors," *J. Raman Spectros.* **25**, 25–29 (1994).
70. R. R. Alfano, C. H. Lui, W. L. Sha, H. R. Zhu, D. L. Akins, J. Cleary, R. Prudente, and E. Cellmer, "Human breast tissues studied by IR Fourier transform Raman spectroscopy," *Lasers Life Sci.* **4**(1), 23–28 (1991).
71. C. J. Frank, D. C. Redd, T. S. Gansler, and R. L. McCreery, "Characterization of human breast biopsy specimens with near-IR Raman spectroscopy," *Anal. Chem.* **66**(3), 319–326 (1994).
72. A. Ferenczy and B. Winkler, "Cervical intraepithelial neoplasia," in *Pathology of the Female Genital Tract*, A. Blaustein, ed., pp. 156–177, Springer-Verlag, New York (1982).
73. C. H. Liu, W. L. Sha Glassman, H. R. Zhu, D. L. Akins, L. I. Deckelbaum, M. L. Stetz, K. O'Brien, J. Scott, and R. R. Alfano, "Near-IR Fourier transform Raman spectrscopy of normal and atherosclerotic human aorta," *Lasers Life Sci.* **4**(3), 257–264 (1992).
74. A. J. Berger, I. Itzkan, and M. S. Feld, "Noninvasive concentration measurements of dissolved analytes in human whole blood by Raman spectroscopy," *American Society of Photobiology* (Presentation only) (1995).
75. I. R. Lewis, N. W. Daniel, Jr., N. C. Chaffin, and P. R. Griffiths, "Raman spectrometry and neural networks for the classification of wood types - 1," *Spectrochimica Acta* **50A**(11), 1943–1958 (1994).
76. M. L. Myrick, S. M. Angel, and R. Desiderio, "Comparison of some fiber optic configurations for measurement of luminescence and Raman scattering," *Appl. Opt.* **29**(9), 1333–1344 (1990).
77. M. L. Myrick and S. M. Angel, "Elimination of background in fiber-optic Raman measurements, *Appl. Spectros.* **44**(4), 565–570 (1990).
78. S. D. Schwab and R. L. McCreery, "Versatile, efficient Raman sampling with fiber optics," *Anal. Chem.* **56**, 2199–2204 (1984).
79. N. T. Yu, J. F. R. Kuck, Jr., and C. C. Askren, "Laser Raman spectroscopy of the lens in situ, measured in an anesthetized rabbit," *Current Eye Res.* **1**(10), 615–618 (1982).
80. ANSI, "Americal National Standards for Safe Use of Lasers," American National Safety Institute, Orlando, FL (1993).
81. F. P. Incropera and D. P. DeWitt, *Fundamentals of Heat and Mass Transfer*, Wiley, New York (1990).
82. J. H. Torres, M. Motamedi, J. A. Pearcr, and A. J. Welch, "Experimental evaluation of mathematical models for predicting the thermal response of tissue to laser irradiation," *Appl. Opt.* **32**(4), 597–606 (1993).
83. J. R. Kramer, Jr., T. J. Romer, J. F. Brennan, III, Y. Wang, R. R. Dasari, and M. S. Feld, "Spectral diagnosis of human coronary artery: Clinical system for real-time analysis," in *Lasers in Surgery: Advanced Characterization, Therapeutics and Systems V,* R. Anderson and A. Katzir, eds., Proc. SPIE **2395**, 376–382 (1995).
84. J. J. Baraga, M. S. Feld, and R. P. Rava, "In Situ optical histochemistry of human artery using near infrared Fourier transform Raman spectroscopy," *Proc. Natl. Acad. Sci. U.S.A.* **89**(8), 3473–3477 (1993).